

Interplay between thermal and compositional gradients decides the microstructure during thermomigration: a phase-field study

Sandip Guin^{†a,b}, Soumya Bandyopadhyay^{†a,c}, Saswata Bhattacharyya^{d,*}, Rajdip Mukherjee^{a,*}

^aDepartment of Materials Science and Engineering, Indian Institute of Technology, Kanpur, Kanpur-208016, UP, India

^bInternational College of Semiconductor Technology, National Yang Ming Chiao Tung University, Hsinchu 300, Taiwan

^cDepartment of Materials Science and Engineering, University of Florida, Gainesville, Florida-32611

^dDepartment of Materials Science And Metallurgical Engineering , Indian Institute of Technology, Hyderabad , Sangareddy - 502285, Telangana, India

Abstract

The presence of thermal gradients in alloys often leads to non-uniformity in concentration profiles, which can induce the thermomigration of microstructural features such as precipitates. To investigate such microstructural changes, we present a phase-field model that incorporates coupling between concentration and thermal gradients. First, we simulated the evolution of non-uniform concentration profiles in the single-phase regions of Fe-C and Fe-N alloy systems due to imposed thermal gradients. To validate our model with the classical experiments performed by Darken and Oriani, we studied the evolution of spatially varying concentration profiles where thermal gradients encompass single-phase and two-phase regions. We developed a parameterized thermodynamic description of the two-phase region of a binary alloy to systematically study the effect of interactions between chemically-driven and thermal gradient-driven diffusion of solute on the evolution of precipitates. Our simulations show how thermal gradient, precipitate size, and interparticle distance influence the migration and associated morphological changes of precipitates. The composition profiles and migration rates obtained from single-particle simulations show an exact match with our analytical model. We use two-particle simulations to show conditions under which thermomigration induces the growth of the smaller particle and shrinkage of the larger one in contrast to the isothermal Ostwald ripening behavior. Our multiparticle simulations show similar behavior during coarsening. Moreover, in the presence of a thermal gradient, there is a shift in the center of mass of the precipitates towards the high-temperature region. Thus, our study offers new insights into the phenomena of microstructure evolution in the presence of thermal gradient.

Keywords: Phase-field Model, Thermomigration, Coarsening, Microstructure

1. Introduction

Thermomigration, also known as the Soret effect or the Ludwig-Soret effect, is the phenomenon wherein a thermal gradient triggers mass transport [1–4]. Ludwig first observed the evolution of concentration gradient in a liquid mixture due to thermal gradient [5]. Later, Soret reported a similar phenomenon in a solution of sodium chloride and potassium nitrate [6]. Thermomigration naturally observed in floating seawater ice where a temperature gradient between seawater and solid ice leads to the removal of salt from the ice [7].

Though initially observed in liquid system, thermomigration is equally important in solid-state microstructural evolution. Thermomigration causes the translation migration of microstructural features such as precipitates, voids and inclusions toward hotter or colder ends subject to a positive entropy production rate. For instance, in nuclear fuel cells, nanosized gas bubbles migrate towards the higher temperature side due to large thermal gradients in the fuel cell [8, 9]. The chemical

potential gradient can be related to the thermal gradient according to $\nabla\mu_T = -S^T c \frac{\nabla T}{T}$, where S^T is the thermotransport coefficient and c denotes the overall concentration of the migrating species [10].

Thermal gradient leads to the development of concentration gradient within a solid single-phase system, where solute migrates from lower to higher temperatures. In an experimental monograph, Darken and Oriani demonstrated evolution of composition gradient in the presence of a thermal gradient in single-phase Fe-C and Fe-N alloy as shown in Figure 1a and Figure 1b, respectively [1]. A temperature range of 622°C to 756°C leads to the evolution of the nitrogen (N) concentration gradient in an α -Fe phase as shown by the solid black line in Figure 1a. The black solid line in Figure 1b illustrates the evolution of the carbon (C) concentration gradient in the α -Fe phase over a temperature range spanning 554°C to 690°C. In both alloys, the initial solute concentration was homogeneous. However, due to the thermal gradient in the material, solute atoms (C & N) migrate toward higher temperature regions, manifesting a gradient in the solute concentration [1].

In a system transitioning from a single-phase to two-phase state, alterations in microstructural development occur due to thermal gradients. In this context, a single-phase to two-phase

*Corresponding Authors

Email addresses: saswata@msme.iitk.ac.in (Saswata Bhattacharyya), rajdipm@iitk.ac.in (Rajdip Mukherjee)

[†]These authors contributed equally to this work

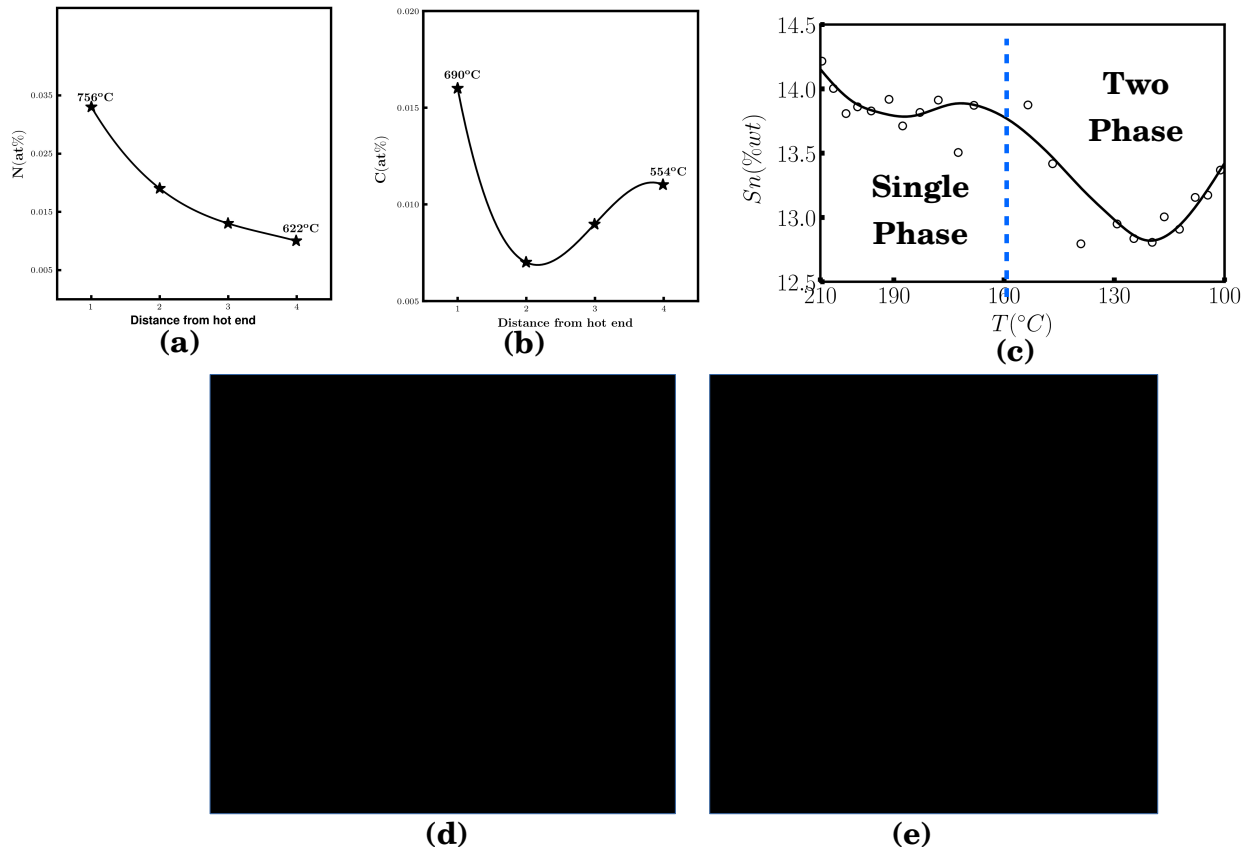


Figure 1: (a) The nitrogen (N) concentration gradient in α -Fe evolves due to the presence of a thermal gradient, as documented by Darken and Orani [1]. (b) Similarly, the carbon (C) concentration gradient in α -Fe system under the influence of a thermal gradient, as reported by Darken and Orani [1]. (c) Sn concentration gradient formation in Pb-Sn alloys under thermal gradient as documented by Steiner [4]. The higher temperature end is in the single-phase region, and the lower temperature end is in the two-phase region [4]. The blue-dotted vertical line separates the single-phase and two-phase regions. (d) Pt-Si droplets migrate on a Si (001) surface, where the periphery of the Si(001) surface has a lower temperature compared to the centre point. Figure will be displayed after publication with permission [11]. (e) Migration of Te precipitates in CdZnTe crystal. Figure will be displayed after publication with permission [12]. The small red circle represents the Te precipitate. Initially located within the region bounded by two solid black lines (shown in the top image), some precipitates have migrated outside this region due to thermal gradient, as indicated in the bottom image. In this case, the left interface of the precipitate matrix has a higher temperature, while the right interface has a lower temperature.

system denotes a material subjected to a thermal gradient where the high-temperature end resides within the single-phase region, while the low-temperature zone exists in the two-phase region. In a classic experiment, Steiner demonstrated the evolution of the concentration gradient for the Pb-Sn system, where he considered the Pb-Sn alloys with an initial Sn concentration of 14 wt% [4]. In this study, the temperature range was 101°C to 210°C. As per the Pb-Sn phase diagram at 14 wt% Sn, above 160°C, the alloy is in the single-phase region, and below that, the alloy is in the two-phase region [4]. Figure 1c shows the final Sn concentration under thermal gradient for Pb-Sn alloy as per the experiment done by Steiner (The blue dotted vertical line separates the single phase from the two-phase region) [4].

In the two-phase system, the second-phase particles exhibit temperature-dependent migration when subjected to a thermal gradient [7]. For example, Zappettini *et al.* used laser-induced thermal gradient to remove Te inclusion in CdZnTe crystal [13]. Another work by Pawar *et al.* investigated the migra-

tion of liquid particles within a solid phase towards the higher temperature, with the equilibrium concentration of the liquid phase being temperature-dependent, while the equilibrium concentration of the solid phase remains constant regardless of the temperature change [14]. Wang *et al.* presented an observation of Pt-Si droplets migrating on a Si (001) substrate driven by a thermal gradient [11]. As shown in Figure 1d, the Pt-Si droplets migrate towards the center of the Si substrate during annealing due to the presence of a thermal gradient between the substrate centre (higher temperature region) and its edge (lower temperature region). Consequently, this thermal gradient generates a Si concentration gradient within the Pt-Si droplets, with higher Si concentration at the higher temperature side. This dictates the droplet migration is due to the “dissolution-diffusion-deposition” flow of Si through the droplets [11]. The experimental observation of Meier *et al.* as shown in Figure 1e, indicates the migration of the Te precipitates (marked as red circles within the two black lines) in CdZnTe crystal due to the pres-

ence of thermal gradient inside the precipitates [12]. In Figure 1e, the top image represents the microstructure before applying the thermal gradient, with Te precipitates represented by red circles within the region shown by two black vertical lines. The bottom image represents the microstructure after applying the thermal gradient. In this case, a thermal gradient is applied using a laser source in such a way that the left interface of the precipitates has a higher temperature while the right interface of the precipitate has a lower temperature. Here it is clearly visible that some precipitates have migrated beyond the region bounded by the two black vertical lines [12].

While the experimental evidence for thermomigration exists in solid-state alloys, there is a scarcity of comprehensive theoretical frameworks [1, 4, 8, 12]. The scientific community must study it adequately after the work done by Darken and Orani [1]. Most studies to date mainly focus on the heat transport coefficient and are limited to void/defects migration; minimal investigation focuses on the possibility of thermomigration arising from equilibrium composition gradient in the precipitate-matrix system [10]. Moreover, no significant approach focuses on the fundamental investigation of the origin of composition gradient due to the presence of thermal gradient as experimentally validated by Darken and Orani. [1]. Furthermore, in two-phase alloys, where temperature variation influences the equilibrium concentrations of both phases (interchange of the equilibrium concentration between solute-rich and solute-poor phases at higher temperatures), frames some open questions, such as how phase migration will manifest in a two-phase alloy characterized by temperature-dependent solubility for both phases under a thermal gradient? Another critical consideration is how this phase migration will impact the process of phase coarsening.

We introduce a phase-field model to answer all these questions. Thus, this study aims to understand the complex synergism of compositional and thermal interactions in different systems. Phase-field modelling serves as a sophisticated computational tool for microstructure simulation, eliminating the need for explicit interface tracking [15]. Its continuous representation of field variables, coupled with a diffuse interface region, facilitates precise simulations of complex microstructural evolution [16–18]. For example, using phase-field modelling, Chakraborty *et al.* studied grain boundary grooving in the presence of both electric current and thermal gradient [19]. Attari *et al.* studied the thermal gradient-driven bonding process in 3D IC solder joint using phase-field simulation [20].

Our analysis starts with studying the thermomigration in a single-phase binary system, following Darken and Orani [1]. We then explore a situation in which we witness a shift from a single-phase to two-phase state, with the higher temperature region constituting the single-phase region and the lower temperature region representing the two-phase region [4]. The simulations related to single-phase and single-phase to two-phase transitions are mainly for validating our simulation results with existing experimental findings. Finally, we study the thermomigration effect in two phase system. We choose precipitate-matrix system for the two-phase system to explore the precipitate migration mechanism through a matrix under a thermal gra-

dient. We also explored the coarsening kinetics of precipitate under a thermal gradient. The following sections demonstrate the implemented model and detailed computational methodology. We report our findings, analysis, and observations in the subsequent sections.

2. Model formulation

2.1. Phase-field formulation

Phase-field modelling presents a simulation technique that enables a straightforward study of microstructural evolution under various conditions [17, 21–23]. In this approach, we consider the interface to have a definite width, and the phase-field parameters change continuously across the width (See the comprehensive reviews by Chen [24], Steinbach [25], etc. for more details). We define the free energy of a system in terms of the phase-field variables, which are subsequently relaxed to equilibrium [26]. Moreover, the temporal evolution of the order parameters ensures the equilibrium, hence mapping the microstructure or morphological changes in different phases [24].

The phase-field model has been used to study various microstructure evolution under external thermal, electrical, and mechanical fields. Using the phase-field method, Mohanty *et al.* studied the diffusion due to thermal gradient [27]. Zhang *et al.* investigated the pore migration under thermal gradient coupled with heat transfer [28]. Recently, Attari *et al.*, using “CALPHAD-reinforced multiphase-field model”, investigated the thermal gradient assisted directional solidification in Cu-Sn micro solder units for rapid bonding in 3-D IC packaging [29]. The effect of interfacial anisotropy on voids/defects migration has also been extensively studied in the last decade [10]. Liang *et al.* investigated the effect of anisotropy in thermal conductivity on the migration of grain boundaries [30]. So, phase-field modelling is an efficient tool for studying microstructure evolution under thermal gradient. Thus, we also use a phase-field model to study the effect of thermal gradient on microstructure evolution.

Let us assume a model system where a precipitate and matrix phase coexist at equilibrium. In this study, we can describe the complete microstructure of the system considering a spatial and temporal distribution of concentration field $c(\mathbf{r}, t)$. Hence, we choose concentration $c(\mathbf{r}, t)$ to be the phase-field variable (conserved), where $\mathbf{r} = (x, y, z)$ denotes the spatial coordinates in the Cartesian frame of reference, and t denotes time. Note that here, we use bold letters to denote the vector fields.

To understand the effect of thermal gradient on mass transport, let us start with the force-flux relationship based on irreversible thermodynamics in a binary system. As already mentioned in this study we have used concentration $c(\mathbf{r}, t)$ as the conserved order parameter; we adopt the Cahn-Hilliard approach in this model [31].

For an isothermal inhomogeneous system, if only the inter-nal process is the redistribution of the chemical species i , mass conservation requires:

$$\frac{\partial c_i(\mathbf{r}, t)}{\partial t} = -\nabla \cdot \mathbf{J}_i, \quad (1)$$

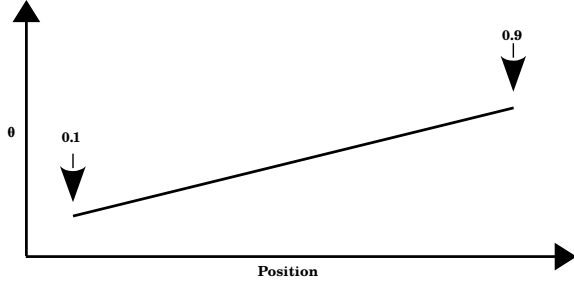


Figure 2: Scaled temperature (θ) profile throughout the domain. Right hand side has high temperature ($\theta_{high}=0.9$) and left hand side has low temperature ($\theta_{low}=0.1$).

where \mathbf{J}_i is the chemical transport flux density. Assuming linear kinetics we have:

$$\mathbf{J}_i = -M_{ij}c_0\nabla\mu_j. \quad (2)$$

Here M_{ij} is the mobility matrix describing the magnitude of the flux density of species i due to the chemical potential gradient of species j , and c_0 defines the average concentration of the system. Combining Equation (1) and Equation (2) we obtain,

$$\frac{\partial c_i(\mathbf{r}, t)}{\partial t} = -\nabla \cdot [-M_{ij}\nabla\mu_j]. \quad (3)$$

In the phase-field model, we describe the quantification of chemical energy dissipation through the evolution of compositional and internal interfacial areas, which is expressed in relation to the overall free energy functional [31]. Thus, we consider the dependency of the local free energy to be not only on the local composition c_i but also on the gradient $\nabla c_i(\mathbf{r}, t)$ as

$$F_{total} = F_{bulk} + F_{gradient}, \quad (4a)$$

$$F_{total} = \int_V [f(c_i(\mathbf{r}, t)) + \frac{\kappa_{c_i}}{2}|\nabla c_i|^2]dV. \quad (4b)$$

Here, we define the total free energy F_{total} as the sum of bulk free energy (F_{bulk}) and the gradient free energy ($F_{gradient}$).

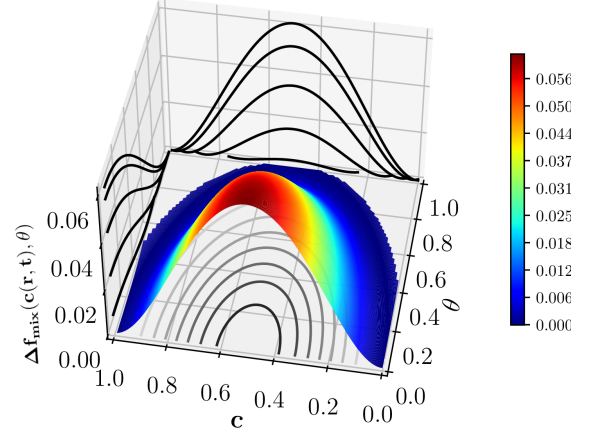
For simplicity, we approximate the gradient energy up to the second order. We describe $f(c_i(\mathbf{r}, t))$ as the bulk free energy density, and κ_{c_i} as the gradient energy coefficient (can be expanded to higher orders to incorporate anisotropy related to crystallographic symmetry) associated with the system.

The chemical potential relative to the final equilibrium state is defined as

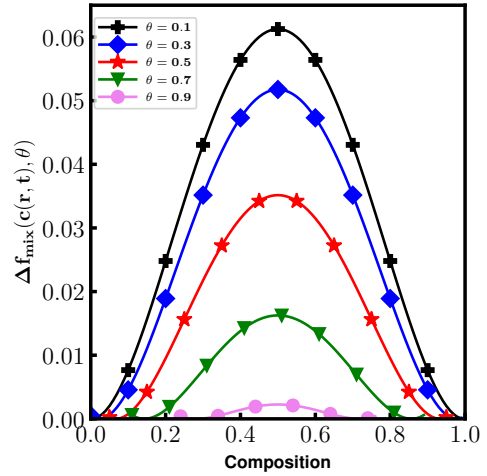
$$\begin{aligned} \mu_i &= \frac{\delta F_{total}}{\delta c_i} \\ &= \frac{\partial f(c_i(\mathbf{r}, t))}{\partial (c_i(\mathbf{r}, t))} - \kappa_{c_i}\nabla^2 c_i(\mathbf{r}, t). \end{aligned} \quad (5)$$

Putting the expression of μ_i (Equation(5)) into Equation (3) we obtain:

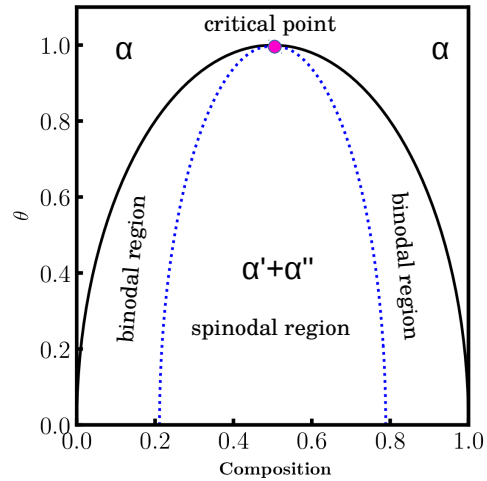
$$\begin{aligned} \frac{\partial c_i(\mathbf{r}, t)}{\partial t} &= -\nabla \cdot \left[-M_{ij}\nabla \frac{\delta F_{total}}{\delta c_i} \right] \\ &= \nabla \cdot M_{ij} \left[\nabla \left(\frac{\partial f(c_j(\mathbf{r}, t))}{\partial (c_j(\mathbf{r}, t))} - \kappa_{c_j}\nabla^2 c_j(\mathbf{r}, t) \right) \right]. \end{aligned} \quad (6)$$



(a) $\Delta f_{mix}(c(\mathbf{r}, t), \theta)$ surface plot



(b) $\Delta f_{mix}(c(\mathbf{r}, t), \theta)$ vs c



(c) phase diagram

Figure 3: (a) Free energy ($\Delta f_{mix}(c(\mathbf{r}, t), \theta)$) surface plot as a function of composition(c) and temperature. (b) ($\Delta f_{mix}(c(\mathbf{r}, t), \theta)$) vs composition (c) at different temperature (θ). (c) Phase diagram derived from ($\Delta f_{mix}(c(\mathbf{r}, t), \theta)$).

In the presence of thermal gradient when mass flow is dictated by the thermo-transport mechanism we rewrite Equation(1) as

$$\frac{\partial c_i(\mathbf{r}, t)}{\partial t} = -\nabla \cdot \mathbf{J}_i - \nabla \cdot \mathbf{J}_Q^i. \quad (7)$$

Here \mathbf{J}_Q^i defines the thermal mass flow density or the thermal flux of the chemical species i . We rewrite \mathbf{J}_Q^i as:

$$\mathbf{J}_Q^i = -\frac{M_{ij}^T Q c_j(\mathbf{r}, t) \nabla T}{T}, \quad (8)$$

where M_{ij}^T is the thermal mobility, T denotes the temperature, and Q is the thermo-transport heat often considered as the change of heat, related to the solute particle transfer between two regions at slightly different temperatures [32, 33]. Considering the unit of Q to be $\frac{J}{mole}$ [34], M_{ij}^T as $\frac{m^2 mole}{Js}$, and c_i to be $\frac{mole}{m^3}$, Equation 8 becomes dimensionally consistent with thermal flux \mathbf{J}_Q^i having unit of $\frac{mole}{m^2 s}$ (similar to \mathbf{J}^i in Equation 2). Thus, the total flux \mathbf{J} can be rewritten as:

$$\begin{aligned} \mathbf{J} &= \mathbf{J}_i + \mathbf{J}_Q^i \\ &= -M_{ij} \nabla \mu_j - \frac{M_{ij}^T Q c_j(\mathbf{r}, t) \nabla T}{T}. \end{aligned} \quad (9)$$

When mass flow vanishes ($\mathbf{J} = 0$) the chemical potential gradient is given as:

$$\nabla \mu_i = -S_{ij}^T c_j \frac{\nabla T}{T}, \quad (10)$$

here, $S_{ij}^T = \frac{M_{ij}^T}{M_{ij}} Q$ is the thermo-transport coefficient and its sign indicates the direction of the flux of the solute. For example positive S_{ij}^T means the solute migration occurs toward the colder terminal [27].

Together Equation (7) and Equation (10) provide the equation for mass transport due to the presence of thermal gradient as:

$$\frac{\partial c_i(\mathbf{r}, t)}{\partial t} = \nabla \cdot M_{ij} \left\{ \left[\nabla \left(\frac{\partial f(c_j(\mathbf{r}, t))}{\partial(c_j(\mathbf{r}, t))} - \kappa_{c_j} \nabla^2 c_j(\mathbf{r}, t) \right) \right] + \left[S_{ij}^T c_j \frac{\nabla T}{T} \right] \right\}. \quad (11)$$

We have discussed earlier that temperature-dependent equilibrium solubility also causes the thermomigration of distinct phases. The primary objective of this paper is to investigate this thermomigration driven by temperature-dependent equilibrium solubility. Thus, we focus on a temperature range where the system is diffusion-dominated (considering higher mass flow) and the effect arising due to the thermal flux \mathbf{J}_Q^i is negligible or assuming $M_{ij}^T \approx 0.0$ in Equation (10). Moreover, we introduce a new model that considers a two-phase solid solution within this temperature range, with the equilibrium solute concentration of each phase as a function of temperature T .

In our simulation we use scaled form of all the variable. For example, we use scaled form of temperature. This scaled temperature is represented by θ . We also assume a linear temperature distribution as shown in Figure 2. We can obtain this the

linear distribution of the temperature by solving steady state heat equation $\nabla \cdot (k_Q \nabla \theta) = 0$, where k_Q denotes the thermal conductivity. In general, k_Q can be composition dependent, but here we have assumed it to be a constant ($k_Q = 1$).

To implement the model, we consider a double well potential for the bulk free energy as:

$$f(c_i(\mathbf{r}, t), \theta) = \Delta f_{mix}(c_i(\mathbf{r}, t), \theta) = A(c_i - c_{eq_i}^m(\theta))^2 (c_i - c_{eq_i}^p(\theta))^2, \quad (12)$$

where, $\Delta f_{mix}(c_i(\mathbf{r}, t), \theta)$ represents the double well potential shown in Figure 3(a), and A is a constant describing the barrier height of the assumed double well potential. For our simulation, we take A to be 1.0.

Figure 3(b) shows the $\Delta f_{mix}(c_i(\mathbf{r}, t), \theta)$ vs composition ($c_i(\mathbf{r}, t)$) diagram for different temperature, where we observe a reduction in the barrier height as a function of temperature. Figure 3(c) shows the corresponding phase diagram of the model. We calculate the phase diagram by computing the solute solubility of both matrix and precipitate phases using the common tangent construction at every temperature.

Further, we formulate the equilibrium compositions for the matrix $c_{eq_i}^m(\theta)$ and precipitate $c_{eq_i}^p(\theta)$ phases as a function of temperature (θ) as:

$$c_{eq_i}^m(\theta) = 0.5 - \sqrt{\frac{1 - \theta^2}{4}}, \quad (13)$$

$$c_{eq_i}^p(\theta) = 0.5 + \sqrt{\frac{1 - \theta^2}{4}}. \quad (14)$$

Finally, the spatio-temporal evolution of the concentration field in the matrix as well as precipitate is governed by the conserved Cahn-Hilliard equation ansatz [24, 31]:

$$\frac{\partial c_i(\mathbf{r}, t)}{\partial t} = \nabla \cdot M_{ij}(c_j(\mathbf{r}, t), \theta) \left[\nabla \left(\frac{\partial f(c_i(\mathbf{r}, t), \theta)}{\partial(c_j(\mathbf{r}, t))} - \kappa_{c_j} \nabla^2 c_j(\mathbf{r}, t) \right) \right], \quad (15)$$

where $M_{ij}(c_i(\mathbf{r}, t), \theta)$ is the mobility of the system which can be composition as well as temperature dependent.

2.2. Finite element discretization of the governing equations

The finite element method (FEM) has been widely used to solve the complex partial differential equations (PDE) with ease for many years by the scientific community due to simplicity in the discretization of the equations into the weak form and efficiently handling the exact boundary conditions. Here we perform a FEM based method to solve the governing phase-field equation (Equation (15)) with proper boundary conditions. Moreover, in our case, the incorporation of the effect of temperature at the boundaries make this problem perfect to solve using FEM with mixed boundary conditions (Neumann, Dirichlet, and Periodic). Figure 4 shows the details of boundary conditions (BC) for our simulation. In the Y-direction, we employ periodic BC for composition (c), chemical potential(μ) and temperature (θ). In the X-direction, we employ no flux condition for both c and μ , while for θ , we employ Dirichlet BC. Although solving the Cahn-Hilliard equation is a bit difficult, due

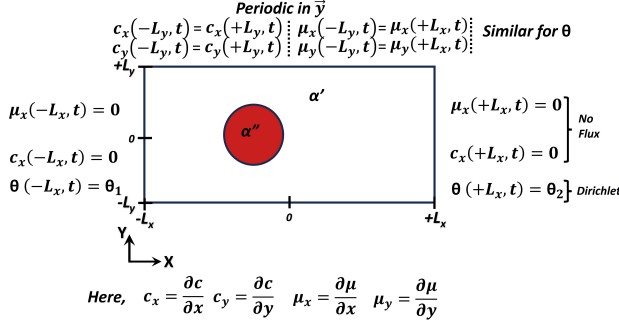


Figure 4: Schematic shows domain boundary condition (BC). Here, c denotes solute concentration, μ is the chemical potential and θ is scaled temperature. In our simulation ($\theta_2 = \theta_{high}$) > ($\theta_1 = \theta_{low}$). In the Y-direction we employ periodic BC for composition (c), chemical potential (μ) and temperature (θ). In the X-direction we employ no flux condition for both c and μ , while for θ , we employ Dirichlet BC.

to the presence of gradient-free energy which is a fourth-order differential equation nevertheless, it can be solved in two ways.

First to prepare for the FEM discretization of Equation (15), we construct a weak form in a similar manner to that used by Stogner et al. [35]. The weighted integral residual projection of Equation (15) is constructed using a test function ϕ_m and integrating the second-order terms by parts once and the fourth order term by parts twice. Thus after discretization Equation (15) yields:

$$\begin{aligned}
 \left(\frac{\partial c_i(\mathbf{r}, t)}{\partial t}, \phi_m \right) &= - \left(\kappa_{c_j} \nabla^2 c_j(\mathbf{r}, t), \nabla \cdot (M_{ij}(c_j(\mathbf{r}, t), \theta) \nabla \phi_m) \right) \\
 &\quad - \left(M_{ij}(c_j(\mathbf{r}, t), \theta) \nabla \left(\frac{\partial f(c_j(\mathbf{r}, t))}{\partial c_j(\mathbf{r}, t)} \right), \nabla \phi_m \right) \\
 &\quad + \langle M_{ij}(c_j(\mathbf{r}, t), \theta) \nabla (\kappa_{c_j} (\nabla^2 c_j(\mathbf{r}, t)) \cdot \hat{n}), \phi_m \rangle \\
 &\quad - \left\langle M_{ij}(c_j(\mathbf{r}, t), \theta) \nabla \left(\frac{\partial f(c_j(\mathbf{r}, t))}{\partial c_j(\mathbf{r}, t)} \right) \cdot \hat{n}, \phi_m \right\rangle \\
 &\quad + \langle \kappa_{c_j} \nabla^2 c_j(\mathbf{r}, t), M_{ij}(c_j(\mathbf{r}, t), \theta) \nabla \phi_m \cdot \hat{n} \rangle,
 \end{aligned} \tag{16}$$

where $(*, *)$ operator represents a volume integral with an inner product and $\langle *, * \rangle$ operator denotes the surface integral with an inner product.

Another way to solve Equation (15) is to split the fourth order equation into two second order equations, such that two variables are solved, the concentration $c_i(\mathbf{r}, t)$ and the chemical potential μ_i . In this case, the two residual equations are:

$$\begin{aligned}
 R_{\mu_i} &= \left(\frac{\partial c_i(\mathbf{r}, t)}{\partial t}, \phi_m \right) + \left(M_{ij}(c_j(\mathbf{r}, t)) \nabla \mu_j, \nabla \phi_m \right) \\
 &\quad - \langle M_{ij}(c_j(\mathbf{r}, t)) \nabla \mu_j \cdot \hat{n}, \phi_m \rangle.
 \end{aligned} \tag{17a}$$

$$\begin{aligned}
 R_{c_i} &= (\nabla c_i(\mathbf{r}, t), \nabla (\kappa_{c_i} \phi_m)) - \langle \nabla c_i(\mathbf{r}, t) \cdot \hat{n}, \kappa_{c_i} \phi_m \rangle \\
 &\quad - \left(\left(\frac{\partial f(c_i(\mathbf{r}, t))}{\partial c_i(\mathbf{r}, t)} - \mu_i \right), \phi_m \right).
 \end{aligned} \tag{17b}$$

In this work we mainly adopt the second or the split formalism

of Equation (17a) & Equation (17b) as this change improves the solve convergence without any impact in the solution.

Thus, we discretize each equation in its weak form in a typical FEM way. All the required FEM objects and architecture are provided by MOOSE [36, 37]. We use a QUAD4 type mesh element to discretize the system. Lagrange shape functions are used for the conserved field variable, chemical potential, and any coupled variables e.g. temperature. The transient system of PDEs is integrated over time implicitly. The system (Equations. (17a)- (17b)) is solved using Newton's method [36, 37] with appropriate boundary conditions shown in Figure 4. Additionally, we assume isotropic and constant values for the mobility ($M_{ij}(c_i(\mathbf{r}, t), \theta) = M_c$) and gradient energy coefficient ($\kappa_{c_i} = \kappa_c$).

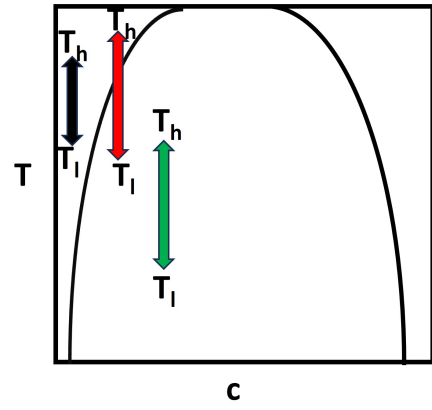


Figure 5: Schematic phase diagram showing three different sets of simulation. The black double-sided arrow shows the case where both high and low temperature is within the single phase region; the red double-sided arrow shows single phase to two-phase case, where high-temperature point is in the single-phase region and the low-temperature point is in the two-phase region. Finally the green double-sided arrow shows the two phase case, where both high and low temperature point is in the two phase region.

3. Model validation and simulation details

3.1. Single-phase system

In this sub section, we cross-reference our simulation outcomes against experimental data pertaining to single-phase system. In the context of a single-phase system, it involves a binary alloy experiencing a thermal gradient where both high and low-temperature points reside within the confines of the single-phase region. Essentially, the entire system remains within this single-phase domain, as visually indicated by the double-sided black arrow in Figure 5. To perform the simulations, we choose a single-phase α -Fe in Fe-C and Fe-N systems following Darken and Orani [1]. More information regarding the simulations for is detailed in Section 1 of the Supplementary Material.

Figure 1a shows the concentration gradient of N (at%) within a temperature range $622^\circ\text{C} \rightarrow 756^\circ\text{C}$. Figure 1b shows the concentration gradient of C (at%) within a temperature region $554^\circ\text{C} \rightarrow 690^\circ\text{C}$. The black and the red lines in both figures

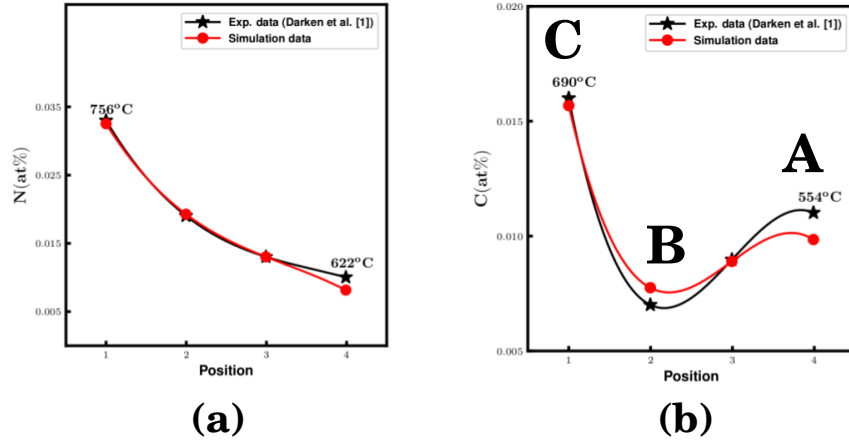


Figure 6: (a) The nitrogen (N) concentration gradient in α -Fe evolves due to the presence of a thermal gradient, as documented by Darken and Orani [1]. (b) Similarly, the carbon (C) concentration gradient in α -Fe undergoes changes under the influence of a thermal gradient, as reported by Darken and Orani [1]. The experimental observations by Darken and Orani are represented by the black line, while our simulation results are depicted by the red line in both cases. In region-A, carbon diffusion comes to a halt due to the low temperature. In region-B, the carbon diffusivity is significant enough to allow solute migration. Consequently, carbon atoms move from region-B to region-A, where the temperature is higher.

correspond to the experimental (done by Darken and Orani [1]) and simulation results, respectively. As observed, our simulation results show a decent agreement between the concentration profiles of carbon (C) and nitrogen (N) within the α -Fe phase and the experimental observations of Darken and Orani under thermal gradient [1].

In the regular solution model, the interplay between the increase in entropy and the enthalpy dictates the overall effect of increasing temperature on the thermodynamics (free energy) of mixing. Thus, for any system, changes in entropy (ΔS), enthalpy (ΔH), and hence free energy (ΔG) are mainly governed by the change in temperature. In general, an increase in temperature increases the entropy or the degree of disorder in a system, which can lead to a decrease in the free energy change of the system, as a higher entropy contribution term ($-T\Delta S$) can compensate for the enthalpy term [38]. This indicates the migration of solute atoms toward higher temperature regions (due to the lower free energy contribution at elevated temperatures), manifesting a concentration gradient in both the C and N inside the α ferrite phase. Figure 6a shows at higher temperatures, N concentration is higher, while at lower temperatures, N concentration is lower.

Figure 6b shows the C concentration remains unchanged at the lower temperature regions (marked as region A in Figure 6b). This is due to the diffusion of C atoms freezes due to lower diffusivity at the lower temperature region [1]. However, in the region where the temperature is sufficient for the diffusion of C atoms (marked as region B in Figure 6b), the atoms start migrating toward the higher temperature region (marked as region C in Figure 6b), which explains the dip in C concentration in the middle of the sample (marked as region B in Figure 6b).

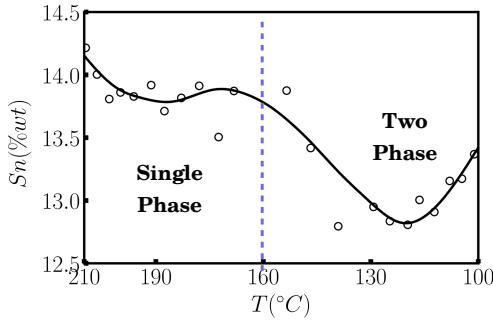
3.2. Single-phase to two-phase system

In this sub-section, we cross-reference our simulation outcomes against experimental data pertaining to single-phase to two-phase systems. Here, the high-temperature point is situated within the single-phase region, while the low-temperature point falls within the two-phase region. This distinction is illustrated by the red arrow in Figure 5.

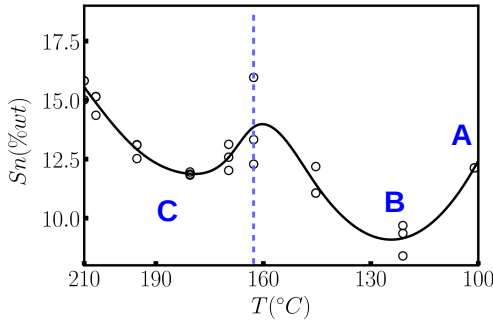
Steiner demonstrated the evolution of the concentration gradient for the Pb-Sn system, where they considered the Pb-Sn alloys with an initial Sn (wt%) concentration of 14 wt% [4]. In their study, the temperature range was 101°C to 210°C. As per the phase diagram at 14 wt% Sn, above 160°C, the alloy is in the single-phase region, and below that, the alloy is in the two-phase region [4]. Figure 7a shows the final Sn concentration after applying thermal gradient as done by Steiner for Pb-Sn alloy [4]. The blue vertical dotted line separates the single phase from the two-phase region.

Figure 7b shows the simulation results for the experiment performed by Steiner [4]. We start our simulations with the initial Sn concentration of around 14 wt%. Note that the initial microstructure of our simulations comprises both two-phase and single-phase regions. Within the single-phase region, the initial concentration of Sn is 14 wt%. Section 2 of the supplementary materials provides detailed simulation information.

With the rise in temperature within the two-phase regions, the Sn solubility of the matrix phase (α) increases, while for precipitate (β) decreases. With time, due to the presence of thermal gradient, the solute within the single-phase region starts migrating toward regions with higher temperatures, resulting in Sn concentration gradient in the single-phase region, akin to the process observed in the case of Fe-N single-phase system as demonstrated by Darken and Orani [1]. Thus, in “Region C” of Figure 7b, we observe a decline in Sn concentration as the so-



(a) Experimental result



(b) Simulation result

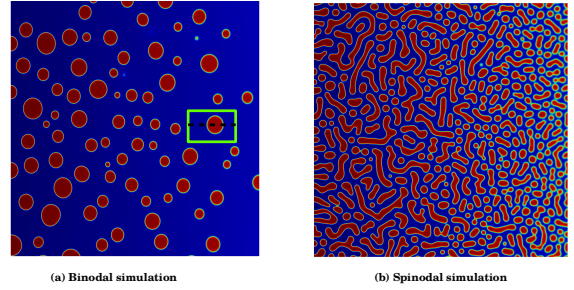
Figure 7: (a) Shows the experimental observation (Sn concentration vs. temperature ($T^{\circ}C$)) done by Steiner for Pb-Sn system in single to two-phase region under a temperature range of $101^{\circ}C$ to $210^{\circ}C$ [4]. (b) Shows the our simulation results (Sn concentration vs. temperature ($T^{\circ}C$)).

lute migrates toward higher temperature regions from this area. Consequently, the precipitate (β) in the two-phase region begins to dissolve, leading to the release of extra solutes. These solutes will subsequently migrate toward the single-phase region. Hence, there is an increase in Sn concentration near the single-phase and two-phase boundary region [4]. As the precipitate dissolves in the two-phase region, the two-phase region becomes a single phase region and in this region a concentration gradient is established.

The region marked as “Region A” in Figure 7b (right-hand side of the plot) corresponds to the lowest temperature region. In this region, the diffusion of solute atoms is arrested, resulting in an unchanged Sn concentration in the region. However, in “Region B”, the diffusivity is adequate to allow the diffusion of solute atoms from this region towards the higher temperature region. As a result, there is a dip in Sn concentration in “Region B” [4].

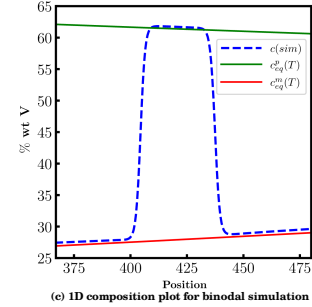
3.3. Two-phase system

We now simulate the microstructure evolution of a two-phase Fe-V system in a thermal gradient where the equilibrium concentration of both phases varies with temperature. In this case,



(a) Binodal simulation

(b) Spinodal simulation



(c) 1D composition plot for binodal simulation

Figure 8: (a) Shows the binodal microstructure evolution for initial composition (C_0) of 29.43 wt % V. (b) Shows the spinodal microstructure evolution for initial composition (C_0) of 29.43 wt % V. (c) 1D composition profile taken along the black dotted line bounded by green rectangular box from the binodal microstructure along with comparison with the equilibrium concentration. Here, the blue line represents the 1D composition plot from the simulation, while the red and green lines represent the equilibrium V concentration in α and σ phase, respectively.

the temperature range is $834^{\circ}C \rightarrow 1056^{\circ}C$. The initial V compositions were 29.43 wt% for the binodal region and 41.66 wt% for the spinodal region [39]. The simulation details are provided in Section 3 of the supplementary document.

Figures 8(a-b) display the corresponding microstructures for the binodal and spinodal compositions. It consists of two phases: one is the solute-poor phase (α), and another one is the solute-rich phase (σ). The equilibrium solute concentration of both α and σ phases are given by the boundary of the miscibility gap in the phase diagram [39]. We observe the formation of the V concentration gradient within each phase as the system has a temperature gradient. We take the 1D solute concentration profile along the black dotted line bounded by a green box in the binodal microstructure. This 1D composition profile is shown in Figures 8c. Here, the red and green lines represent the equilibrium V concentration for α and σ phases (calculated using the Fe-V phase diagram). Here, due to the presence of a thermal gradient, the V concentration, with time, will try to maintain the equilibrium value at each temperature in both phases. As a result, it is visible from Figure 8c, that the V concentration in the α phase nearly follows the red line (equilibrium V concentration of α phase), while the V concentration within the σ phase follows the green line (equilibrium V concentration of σ phase). Here, the V concentration is slightly higher in both phases wrt. to the equilibrium concentration. The circular shape of the σ gives rise to the curvature effect, which is also responsible for the observed increase in equilib-

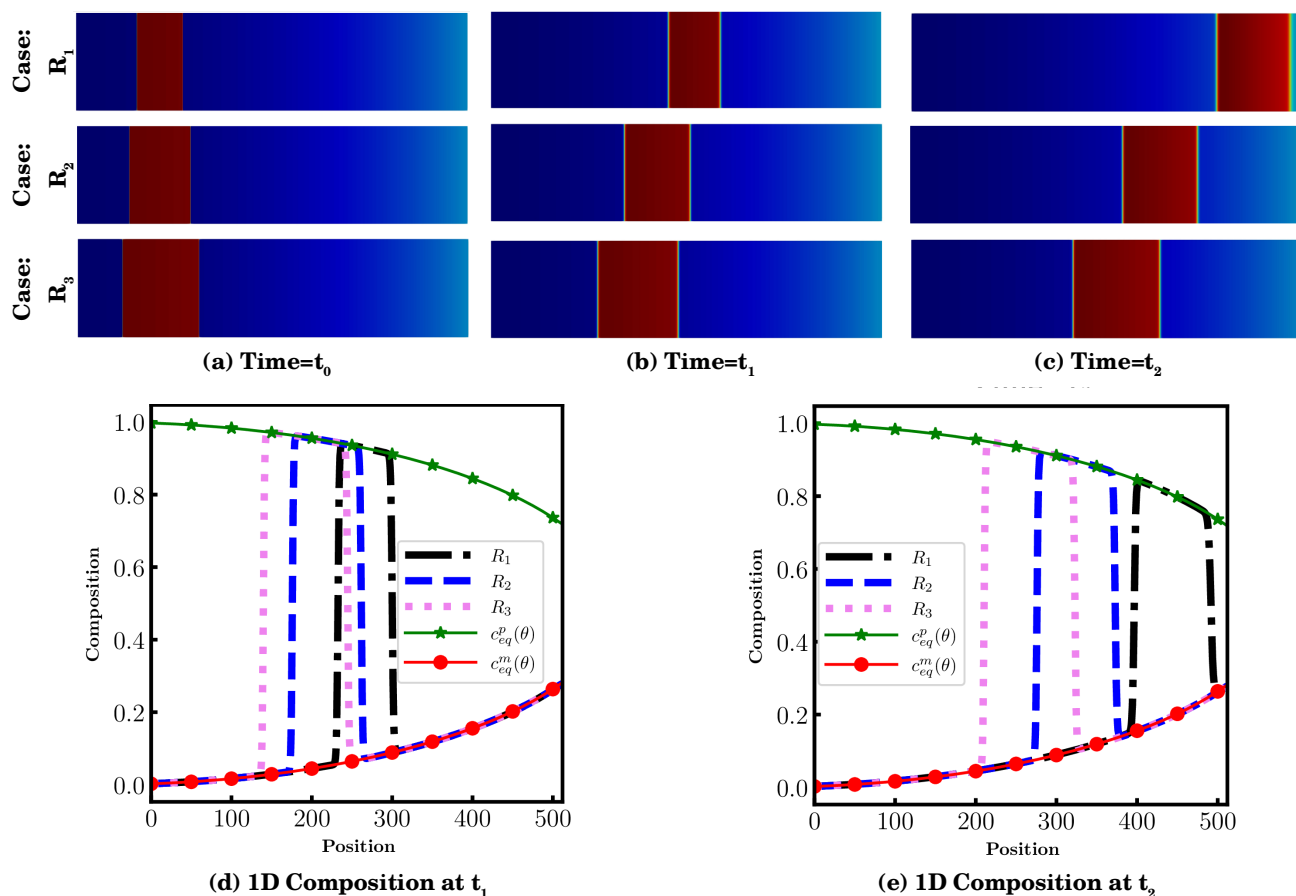


Figure 9: Microstructure evolution of single flat interface precipitate simulation for all three cases (R_1 to R_3 : top to bottom) at (a) $time = t_0$ (initial time), (b) $time = t_1$, and (c) $time = t_2$. The red region is the precipitate, and the remaining blue region is the matrix phase. In all these simulations right end has the highest temperature, while the left end has the lowest temperature. 1D composition plot taken at $y = \frac{m}{2}$ for all three cases along with analytical ($c_{eq}^p(\theta)$) and ($c_{eq}^m(\theta)$) at (c) $time = t_1$ and (d) $time = t_2$. Here, $t_0 < t_1 < t_2$.

rium concentration [40].

The simulations with thermal gradient in a two-phase system show that a thermal gradient creates a concentration gradient inside each phase because of the temperature-dependent equilibrium concentration of phases. However, if the thermal gradient continues to exist even after establishing the concentration gradient, it raises another important question: how does the microstructure evolve in this scenario?

To address this query, we have selected a two-phase precipitate-matrix system for our simulations. The simulations are classified into three different categories:

1. Single precipitate inside a matrix:
 - (a) Precipitate with flat interface (Case: R_1 , R_2 and R_3).
 - (b) Circular precipitate (Case: C_1 , C_2 and C_3)
2. Two circular precipitates with different inter-precipitate distances (Case: A , B and C).
3. Multiple circular precipitates in a matrix.

Table 1: Parameter details of the simulation model described in Section 2.

Parameters	Values
A	1.0
M_c	1.0
κ_c	1.0
θ_{low}	0.1
θ_{high}	0.9
k_Q	1.0
ΔX	0.5
ΔY	0.5

Starting here, our streamlined phase-field model (outlined in Section 2) is employed for efficient thermomigration analysis in a two-phase system. The parameter details are provided in Table 1. Note that in all cases, we consider the initial concentration to be the equilibrium solute concentration ($c_p^{eq}(\theta)$) and

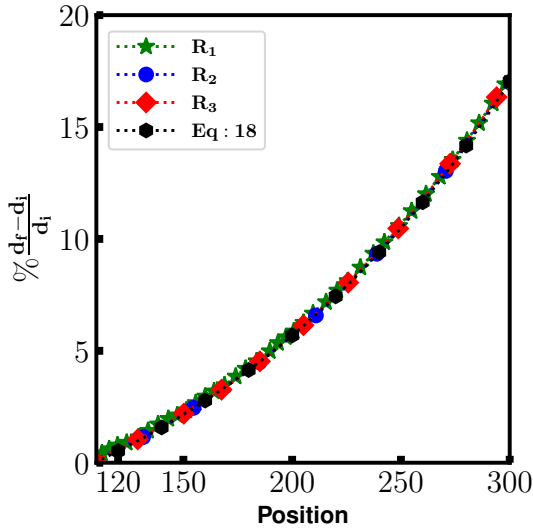


Figure 10: % change in precipitate size wrt. initial size and comparison with Equation 18 for all three flat interface single precipitate simulation cases (R_1 , R_2 and R_3). % change in precipitate size wrt. initial size for all three cases is the same and aligned with the theoretical calculations given by Equation 18.

$c_m^{eq}(\theta)$ for the precipitate and the matrix phases, respectively) as a function of temperature (spatially dependent) for each phase. From here onward, the right-hand side of the simulation domain has the highest temperature ($\theta_{high} = 0.9$), while the left end has the lowest temperature ($\theta_{low} = 0.1$) as shown in Figure 2. We provide detailed explanations for each simulation in the following.

4. Results and Discussions

4.1. Single Precipitate

We initially focus on a single precipitate model to eliminate the influence of inter-precipitate interactions. We examine two configurations: (a) an infinitely long precipitate in the Y direction having flat interface and (b) a circular precipitate. In both cases, we conduct three sets of simulations with varying sizes of precipitates. The simulation sets for the flat interface precipitate are denoted as R_1 , R_2 , and R_3 , while for the circular precipitates, we label them as C_1 , C_2 , and C_3 . The temperature range and total domain size remain consistent throughout all six cases, as specified in Table 2. The only variation lies in the size of the precipitates, which increases from R_1 to R_3 and C_1 to C_3 . Table 3 contains a comprehensive summary of the initial positions and sizes of the single precipitate cases. For flat interface precipitates, the size corresponds to the width in the x -direction, while for circular precipitates, the size corresponds to the diameter of the precipitate.

4.1.1. Flat interface precipitate

We consider an initial flat interface precipitate embedded in a matrix to eliminate the effects associated with curvature [40].

Figure 9(a) depicts the initial configuration of the flat interface precipitates for three cases, with R_1 positioned at the top and R_3 at the bottom. The red region is the precipitate, while the blue colour region is the matrix phase. The initial position of the precipitate is consistent across all cases. Subsequently, Figures 9(b-c) depict the morphological changes observed at later time steps. As the system evolves, we observe the migration of the precipitate toward the region of higher temperature. As mentioned earlier (in Section 3.1), as the temperature increases, the free energy in a system decreases, leading to the migration of solute atoms toward higher-temperature regions.

Analysis of the free energy versus composition plots at different temperatures (Figure 3(b)) shows that a two-phase system exhibits lower free energy value at the higher temperature. Thus, in a two-phase system subjected to a thermal gradient, the state with the minimum free energy would involve the equilibrium of the two phases at the highest temperature point. In our case, the region with the highest temperature is on the right side. Hence, the precipitate initiates migration towards the higher temperature regions to achieve the configuration corresponding to the lowest free energy. During this migration, the precipitate-matrix interface must maintain the equilibrium solute concentration at each temperature, as illustrated by the phase diagram in Figure 3(c). This equilibrium condition corresponds to the minimum free energy configuration at that particular temperature. However, the final minimum free energy configuration corresponds to the precipitate-matrix equilibrium at the highest temperature.

We compare the evolution of a one-dimensional (1D) composition profile, taken along the centre position of the vertical axis, with the equilibrium compositions of the matrix ($c_{eq}^m(\theta)$) and the precipitate ($c_{eq}^p(\theta)$). Remarkably, we observe a perfect agreement in the composition evolution between the precipitate and matrix phases during the migration process, aligning with the analytical equilibrium compositions. Since here we consider the precipitate with the flat interface, the curvature effect is absent, resulting in a perfect equilibrium between solute concentration and temperature throughout the evolution. Figures 9(d-e) illustrate the evolution of 1D composition at times t_1 and t_2 , along with the corresponding equilibrium compositions $c_{eq}^m(\theta)$ and $c_{eq}^p(\theta)$.

As the temperature increases, the equilibrium solute concentration of the precipitate phase ($c_{eq}^p(\theta)$) decreases, while for the matrix phase ($c_{eq}^m(\theta)$) it increases. Let's consider a precipitate initially at position X_i with a corresponding temperature of θ_i . During a small time interval (Δt), the precipitate migrates to a new position (X_f) with a corresponding higher temperature of θ_f ($\theta_f > \theta_i$), where $(X_f - X_i)$, $(\theta_f - \theta_i)$, and Δt are very small. At θ_f , for the precipitate phase the equilibrium solute concentration ($c_p^{eq}(\theta = \theta_f)$) is lower than the equilibrium solute concentration ($c_p^{eq}(\theta = \theta_i)$) at θ_i because $\theta_i < \theta_f$. So, as the precipitate migrates from temperature θ_i to θ_f , it must reject the excess solute ($c_p^{eq}(\theta = \theta_i) - c_p^{eq}(\theta = \theta_f)$) to maintain equilibrium at the new temperature θ_f . This rejection of solute leads to a supersaturated state in the adjacent matrix. Consequently, this extra solute re-enters into the precipitate from the supersaturated matrix, facilitating the growth of the precipitate. Now, the precipi-

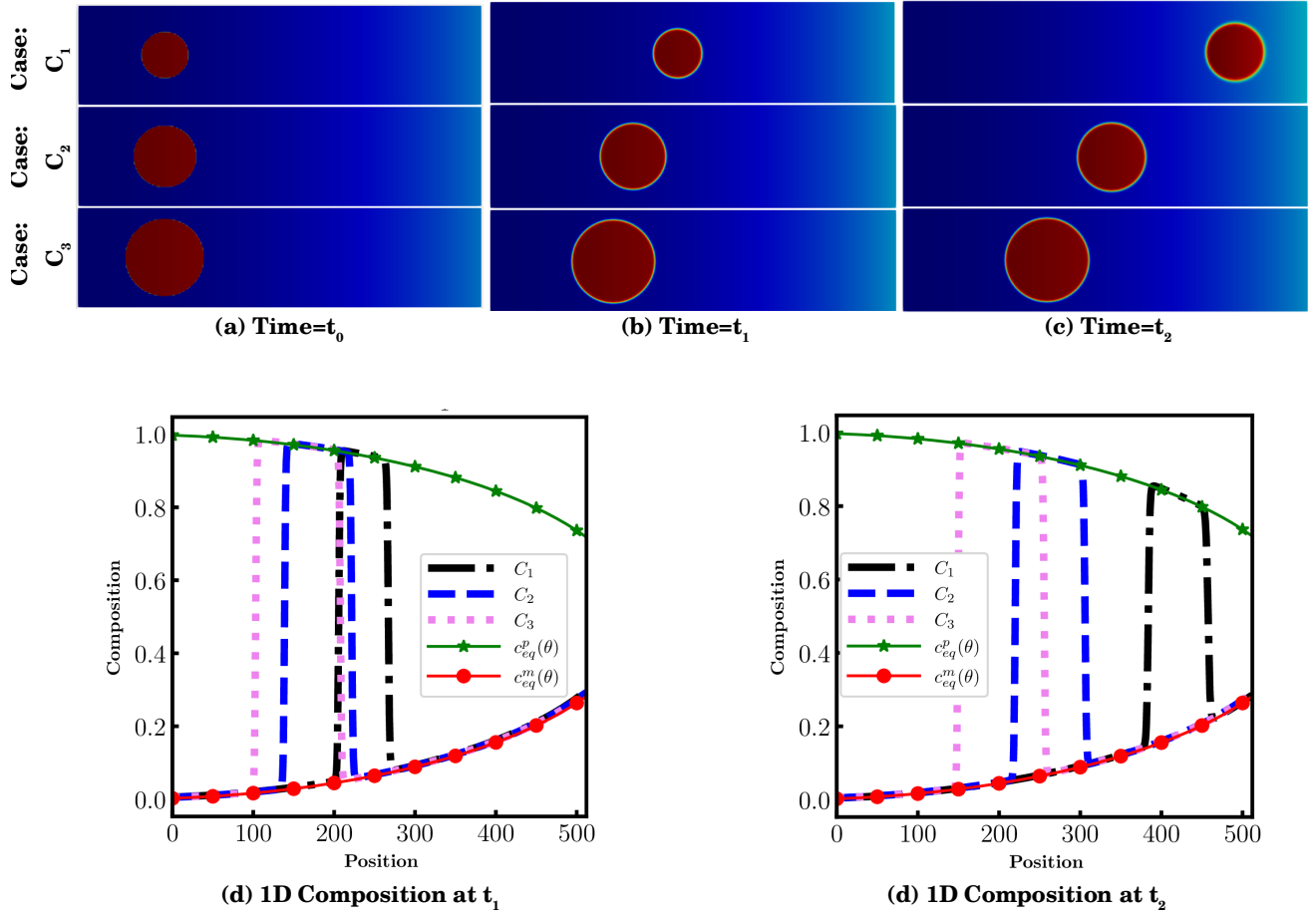


Figure 11: Microstructure evolution of single circular precipitate simulation for all three cases (C_1 to C_3 : top to bottom) at (a) $time = t_0$ (initial time), (b) $time = t_1$, and (c) $time = t_2$. The red region is the precipitate, and the remaining blue region is the matrix phase. In all these simulations, the right end has the highest temperature, while the left end has the lowest temperature. 1D composition plot taken at $y = \frac{m}{2}$ for all three cases along with analytical ($c_{eq}^p(\theta)$) and ($c_{eq}^m(\theta)$) at (c) $time = t_1$ and (d) $time = t_2$. Here, $t_0 < t_1 < t_2$.

tate and matrix phases have attained equilibrium concentration at this new elevated temperature, accompanied by a growth in the precipitate size. The precipitate is now ready to migrate to the next higher temperature stage. This sequence of events will repeat at each temperature during migration, and the size of the precipitate will increase during the migration.

The percentage change in size of the precipitate with respect to its initial size, as the migration occurs, can be calculated using Equation. 18.

$$\frac{d_f - d_i}{d_i} = \left\{ \frac{(c_{eq}^p(\theta = \theta_i^c) - c_{eq}^m(\theta = \theta_i^c))}{(c_{eq}^p(\theta = \theta_f^c) - c_{eq}^m(\theta = \theta_f^c))} - 1 \right\} \times 100, \quad (18)$$

here d_i denotes the initial precipitate size at the onset of thermomigration, θ_i^c signifies the central temperature point at the initial time, d_f represents the final precipitate size following migration, and θ_f^c corresponds to the new central temperature point. The comprehensive derivation of Equation 18 is outlined in Appendix A. Moreover, we compare the percentage

size changes in all three scenarios (R_1, R_2, R_3) in our simulations with the analytical solution. A precise alignment is observed between the percentage size changes in the simulations and those derived from the analytical solution (Equation 18), as depicted in Figure 10.

4.1.2. Circular Precipitate

Figure 11(a) displays the initial setups of the circular precipitate-matrix systems, increasing in diameter from top to bottom (C_1 to C_3). The initial position of the precipitate is consistent across all cases. Subsequently, Figures 11(b-c) depict the morphological changes observed at later time steps. As the system evolves, we observe the migration of the circular precipitate toward the region of higher temperature. We compare the evolution of the one-dimensional (1D) composition profile, taken along the center position of the vertical axis, with the equilibrium compositions of the matrix ($c_{eq}^m(\theta)$) and the precipitate ($c_{eq}^p(\theta)$) (shown in Figures 11(d-e)). Figures 12(a-d) rep-

Table 2: Simulation details for single, two and multi precipitate system.

Dataset	Single Precipitate		Two Precipitates	Multiple Precipitates
	Circular	Flat interface	Circular	Circular
Domain Size	$1024\Delta X \times 256\Delta Y$	$1024\Delta X \times 256\Delta Y$	$1024\Delta X \times 256\Delta Y$	$1024\Delta X \times 1024\Delta Y$
θ	0.1 – 0.9	0.1 – 0.9	0.1 – 0.9	0.1 – 0.9
Case	R_1, R_2, R_3	C_1, C_2, C_3	A, B, C	-

Table 3: Details regarding the initial size and centre position of precipitate for both single flat interface and circular precipitate simulations.

Case	Size	Centre position	Shape of precipitate
R_1	60	(110, 64)	flat interface
R_2	80	(110, 64)	flat interface
R_3	100	(110, 64)	flat interface
C_1	60	(110, 64)	Circular
C_2	80	(110, 64)	Circular
C_3	100	(110, 64)	Circular

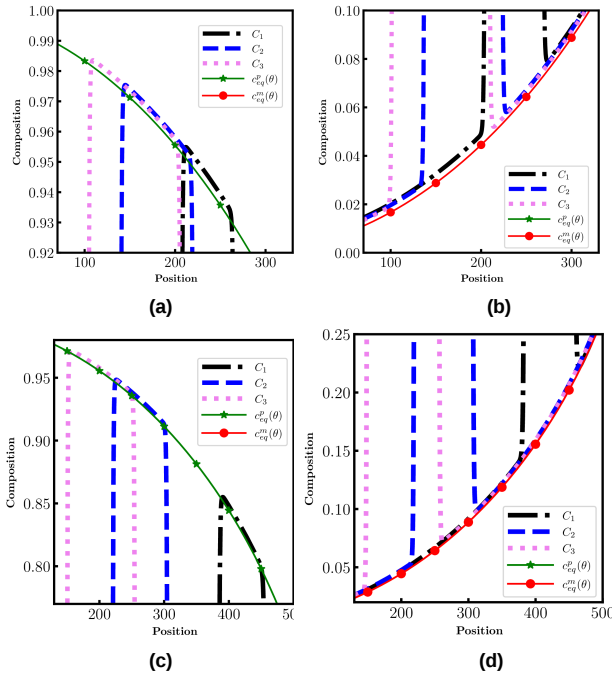


Figure 12: Enlarge view of 1D composition plot for all three circular single precipitate along with analytical ($c_{eq}^p(\theta)$) and ($c_{eq}^m(\theta)$). (a) Showing the 1D composition inside precipitate along with ($c_{eq}^p(\theta)$) at time = t_1 . (b) Showing the 1D composition at matrix adjacent to precipitate along with ($c_{eq}^m(\theta)$) at time = t_1 . (c) Showing the 1D composition inside precipitate along with ($c_{eq}^p(\theta)$) at time = t_2 . (d) Showing the 1D composition at matrix adjacent to precipitate along with ($c_{eq}^m(\theta)$) at time = t_2 .

resent the enlarged view of the 1D composition plot. In Figures 12(a-b), the composition plots depict the solute concentrations of the precipitate and matrix, respectively, at time t_1 , while Figures 12(c-d) showcase the same at time t_2 . At t_1 and t_2 , the

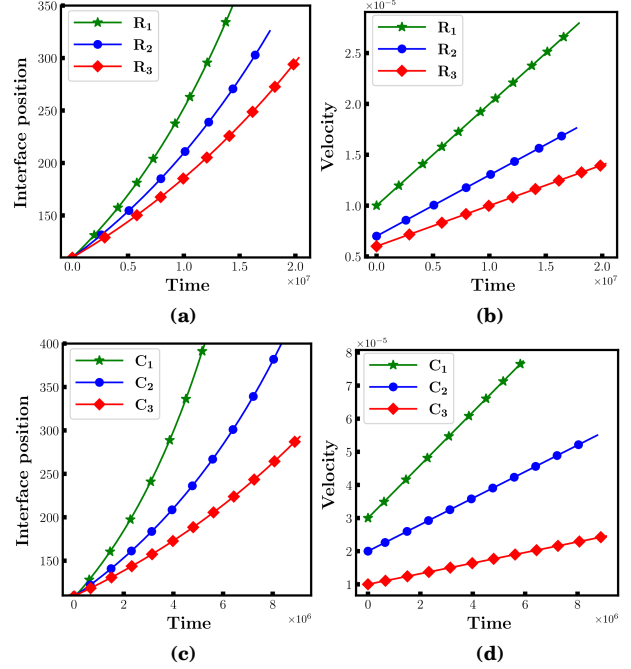


Figure 13: (a) Comparison of precipitate position with time for all three flat interface single precipitate simulations (Case: R_1, R_2 , and R_3). (b) Comparison of migration velocity with time for all three flat interface single precipitate simulations (Case: R_1, R_2 , and R_3). (c) Comparison of precipitate position with time for all three circular single precipitate simulations (Case: C_1, C_2 , and C_3). (d) Comparison of migration velocity with time for all three circular single precipitate simulations (Case: C_1, C_2 , and C_3). For both flat interface and circular precipitate, the velocity increases linearly with time.

solite concentrations of both matrix and precipitate phases are slightly elevated compared to the equilibrium solute concentration ($c_{eq}^p(\theta)$ and $c_{eq}^m(\theta)$). The circular shape of the precipitate gives rise to the curvature effect, which is also responsible for the observed increase in equilibrium concentration for our simulation wrt. $c_{eq}^p(\theta)$ and $c_{eq}^m(\theta)$ [40].

4.1.3. Velocity

The observation of microstructural evolution in both flat interface (Figures 9(a-c)) and circular (Figures 11(a-c)) precipitates reveals that smaller precipitates migrated larger distance for same amount of time compared to larger ones. The smaller precipitate (R_1, C_1) exhibits the fastest migration velocity, followed by moderate velocity for R_2, C_2 , and the slowest velocity for R_3, C_3 . Figure 13(a) illustrates the temporal evolution of the

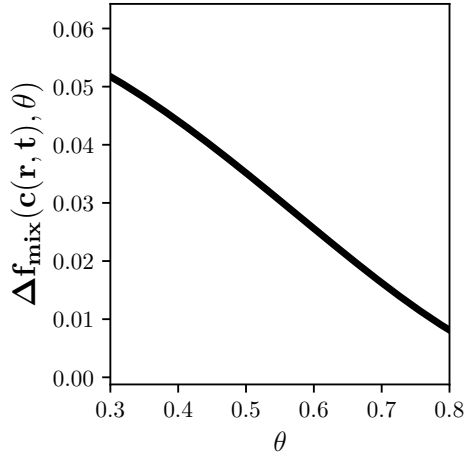


Figure 14: $\Delta f_{mix}(c_i(\mathbf{r}, t), \theta)$ vs θ at $c=0.5$, showing linear reduction in $\Delta f_{mix}(c_i(\mathbf{r}, t), \theta)$ with increasing temperature (θ).

precipitate positions, while Figure 13(b) displays the velocity of the precipitate over time for all three single flat interface precipitates. Figures 13(c-d) display the exact quantities but for a circular precipitate. Notably, the migration velocity consistently increases over time at a constant rate as the precipitates migrate towards the higher-temperature region (shown in Figures 13(b and d)). The green line in these figures represents the velocity of the smaller precipitate, while the red line represents the velocity of the larger precipitate. As the precipitate migrates due to thermal gradient, it has to redistribute the excess solutes (resulting from the decrease in equilibrium solute concentration of precipitate with increasing temperature as explained in Appendix A) at each temperature to maintain equilibrium. The amount of total excess solute depends on the size of the precipitate. As a result, the smaller precipitate requires less time to achieve equilibrium at each temperature during migration by redistributing excess solutes (the total amount of excess solute for smaller precipitate is less than for the large precipitate). This disparity in solute redistribution time is the reason for the higher velocity observed in smaller precipitates than that in larger ones.

Figure 14 shows the correlation between $\Delta f_{mix}(c_i(\mathbf{r}, t), \theta)$ vs θ for a concentration of 0.5. It is apparent that, in the given temperature range, the $\Delta f_{mix}(c_i(\mathbf{r}, t), \theta)$ exhibits an almost linear decline with increasing temperature. In our specific scenario, a linear temperature gradient was applied throughout the entire domain, resulting in a linear proportional decrease in $\Delta f_{mix}(c_i(\mathbf{r}, t), \theta)$ with distance. This linear reduction in $\Delta f_{mix}(c_i(\mathbf{r}, t), \theta)$ acts as the propelling factor for the migration of the precipitate. As the linear reduction in $\Delta f_{mix}(c_i(\mathbf{r}, t), \theta)$ remains consistent across temperature and distance, the precipitate experiences a steady acceleration, resulting in a uniform velocity increase as depicted in Figure 13(b) (for flat interface precipitate) and Figure 13(c) (for circular precipitate).

4.2. Two precipitates

In the preceding section, we obtained valuable insights into thermomigration phenomena in single precipitates of both flat interface and circular configurations. However, real microstructures consist of multiple precipitates of varying sizes, leading to Ostwald ripening [41–43]. So, it becomes essential to investigate the combined effects of Ostwald ripening and thermomigration on microstructure evolution. In the following sections, we present a comprehensive study that delves into the intricate interplay between coarsening and thermomigration of precipitates.

We initiate our study by examining a system composed of two identical circular precipitates with a diameter of 70 units embedded within a matrix. The system consists of two circular precipitates, namely P_1 (located on the colder side) and P_2 (located on the hotter side). We explore the impact on coarsening behaviour by varying the distance between the two precipitates (d_{inter}). Specifically, while keeping the position of P_1 fixed, we alter the center position of P_2 , resulting in three distinct cases labelled as A, B, and C. Here, position refers to the center point of a precipitate. Table 4 presents detailed simulation parameters for each case.

Table 4: Two precipitate simulations details.

Case	Position of P_1	Position of P_2	d_{inter}
A	(50, 64)	(130, 64)	80
B	(50, 64)	(180, 64)	180
C	(50, 64)	(230, 64)	130

4.2.1. Case:A

In Case A, we examine a scenario where the inter-precipitate distance (d_{inter}) between P_1 and P_2 is extremely small. This configuration leads to the observation of shrinkage of P_2 and a slight migration towards the hotter side for both precipitates, as depicted in Figures 15(a-d). The presence of a thermal gradient induces migration in both precipitates. Nevertheless, the precipitate closer to the higher temperature terminal (P_2), undergoes faster migration than P_1 . This temporal precedence occurs for a certain duration. As discussed in the previous section regarding single precipitate simulations, both precipitates release solute into the adjacent matrix during migration to maintain equilibrium concentration with the new temperature. However, in this Case, some of the solute rejected by P_2 in the inter-precipitate region is consumed by P_1 as it migrates to the higher temperature side. The transformation in the shape of P_1 is evident in Figures 15(a-d). Consequently, the size of P_1 initially increases more than that of P_2 . Subsequently, coarsening of P_1 and shrinking of P_2 occur due to the size differences, facilitated by the Gibbs-Thomson effect.

4.2.2. Case:C

In the case of Case : C, we consider a large inter-separation distance (d_{inter}) between P_1 and P_2 . We observe a shrinkage in P_1 and coarsening of P_2 , accompanied by the migration of

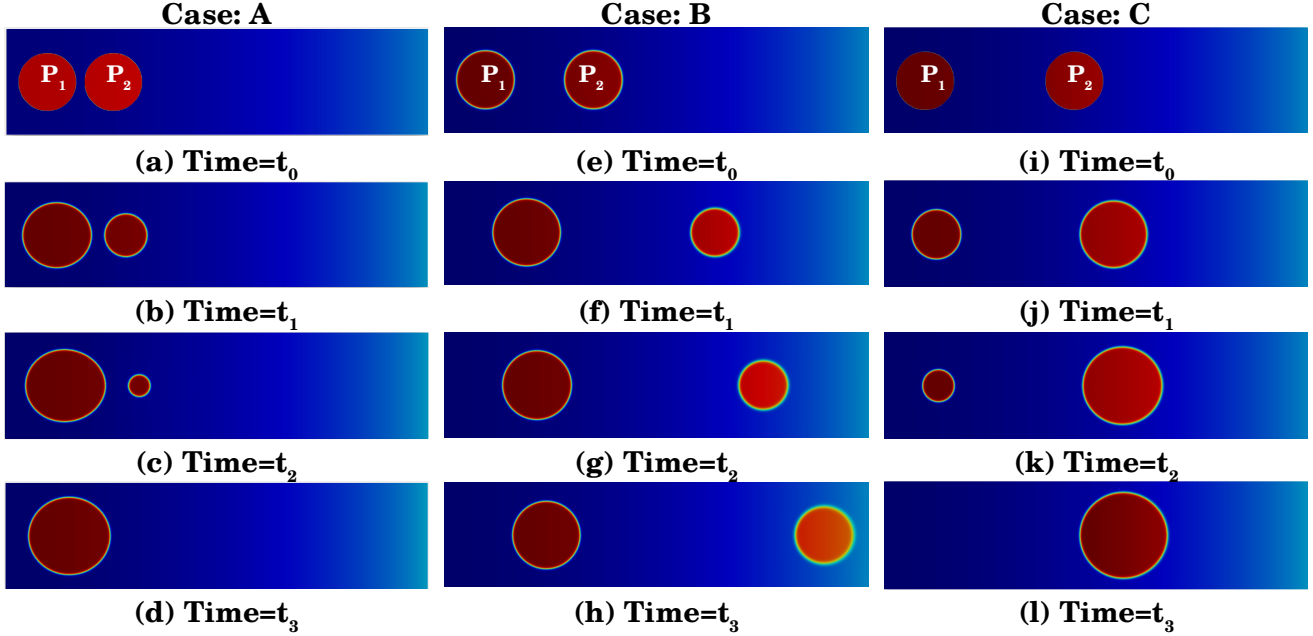


Figure 15: Microstructure evolution for two precipitates simulation for Case:A (d_{imer} is small) at (a) $time = t_0$, (b) $time = t_1$, (c) $time = t_2$ and (d) $time = t_3$. In Case:A, P_1 grows and P_2 shrinks with time. Microstructure evolution for two precipitates simulation for Case:B (d_{imer} is medium) at (e) $time = t_0$, (f) $time = t_1$, (g) $time = t_2$ and (h) $time = t_3$. In Case:B, initially p_2 shrinks but after some time its starts to grow. Microstructure evolution for two precipitates simulation for Case:C (d_{imer} is large) at (i) $time = t_0$, (j) $time = t_1$, (k) $time = t_2$ and (l) $time = t_3$. In Case:C, P_1 shrinks and P_2 grows with time.

P_2 towards the hotter side (shown in Figures 15(i-l)). The thermal gradient present in the system induces migration for both precipitates.

Throughout the migration process, each precipitate rejects excess solute into the surrounding matrix to establish equilibrium with the new temperature. In contrast to *Case : A*, most of the solute rejected by P_2 is absorbed by P_2 itself due to the substantial inter-precipitate distance. Two primary factors contribute to the larger size of P_2 compared to P_1 . Firstly, the higher temperature of P_2 is crucial, as indicated by Equation 14, which illustrates the temperature-dependent equilibrium solubility of the precipitate ($c_{eq}^p(\theta)$). This equation reveals that at elevated temperatures, the change in equilibrium solute concentration wrt. temperature is more pronounced than at lower temperatures. Consequently, even for the same migration distance, the total solute rejected by P_2 precipitate surpasses that of P_1 .

Additionally, due to its higher temperature location, P_2 precipitates migrate at a faster rate than P_1 . Consequently, over the same duration, P_2 covers a greater distance, resulting in a more substantial temperature change and, consequently, increased excess solute rejection. The combination of these two factors leads to P_2 rejecting more excess solute than P_1 .

Moreover, because of the considerable inter-precipitate distance, most of the solute rejected by P_2 re-enters the P_2 precipitate itself. This phenomenon causes a more pronounced increase in the size of the P_2 precipitate. Subsequently, the noticeable size disparity between the two precipitates leads to the larger precipitate (P_2) coarsening at the expense of the smaller precipitate (P_1).

4.2.3. Case:B

For *Case : B*, we consider the inter-separation distance between P_1 & P_2 to be moderate. Initially, we observe a shrinkage in P_2 and coarsening of P_1 along with its migration towards the hotter side (shown in Figures 15(e-g)) region, which is similar to *Case : A*. But as the system evolves, the velocity of P_2 increases because of both high temperature and smaller size compared to P_1 . So, the inter-precipitate distance increases with time. After a certain point, the distance becomes sufficient for the rejected solute to re-enter into the P_2 itself (similar to *Case:C*). For higher temperatures, the equilibrium solute concentration change is more than lower temperatures for the same amount of temperature change. So, as P_2 is on the higher temperature side, the change in equilibrium concentration with the temperature inside the precipitate is higher than P_1 , which is on the lower temperature side. So, even for the same amount of migration, P_2 will grow more than P_1 as displayed in Figures 15(g-h). It is visible that, up to $time=t_2$, the size of P_2 decreases while the P_1 increases. At $time=t_2$ size of P_2 , the precipitate is smaller than the P_1 precipitate. But after $time=t_2$, the size of the P_2 starts to grow. This growth of smaller precipitate (inverse coarsening) is opposite to the conventional Ostwald-ripening behaviour. The evolution of each precipitate size with time is provided in Section 4 of the supplementary material.

4.3. Multiple precipitates

In this section, we extend our model to investigate the behaviour of multiple circular precipitates within a matrix. We

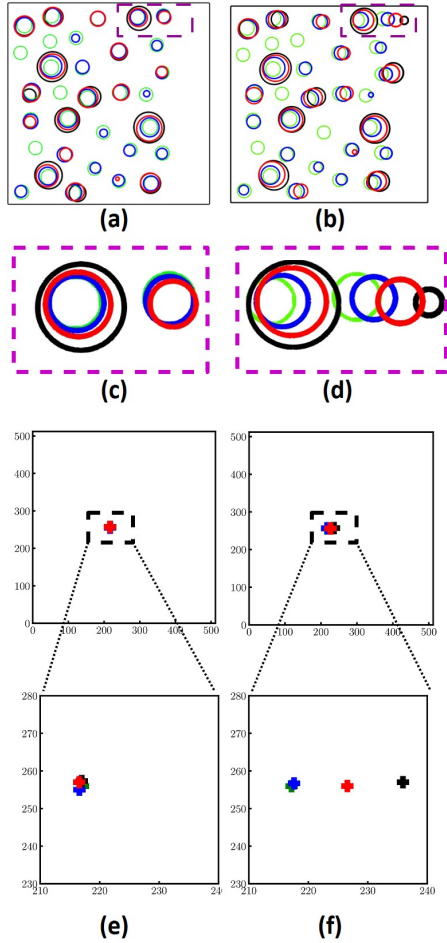


Figure 16: Contour plot of precipitate matrix interface with time for (a) isothermal, (b) with thermal gradient at four different times (t_0, t_1, t_2 , and t_3). Here, $t_0 < t_1 < t_2 < t_3$. Enlarged view of the flat interface section for (c) isothermal case and (d) with thermal gradient case. Average centre (C_{avg}) position of precipitates with time for (e) isothermal, (f) with thermal gradient. The plus signs of different colours represents the C_{avg} for different times. Green colour to represent $time = t_0$, blue colour for $time = t_1$, red colour for $time = t_2$ and black colour for $time = t_3$.

start our multiple precipitates simulations, carefully arranging their initial positions to prevent overlap. The sizes of the precipitates vary between 17 and 20 units, and they are positioned randomly within a $1024\Delta X \times 1024\Delta Y$ matrix. We perform two simulations, one under isothermal condition and another with an existing thermal gradient spanning 0.1 to 0.9. In the isothermal simulation, we set the temperature precisely at half the temperature range within the thermal gradient, specifically $\theta = 0.5$. The microstructural evolution is shown in Figure 16(a) for the isothermal case and Figure 16(b) for the thermal gradient case. Here, we plotted the contour lines representing the precipitate-matrix interface. The green contours denote the initial configuration at t_0 , the blue contours represent the microstructure for at t_1 , the red contours for time t_2 , and the black contours for time t_3 . Note that $t_0 < t_1 < t_2 < t_3$.

In the case of isothermal conditions, shown in Figure 16(a),

we observe normal coarsening phenomenon over time. Larger precipitates coarsen, while smaller precipitates shrink. However, in the presence of a thermal gradient, as the system evolves, the precipitates closer to the higher temperature region initiate migration due to the defined temperature gradient. In contrast, normal Gibbs-Thomson coarsening governs the behaviour of precipitates located in the lower temperature regime. The microstructures during the later stages demonstrate the phenomena above, as shown in Figure 16(b). As the precipitates in the high-temperature regions undergo migration, they encounter changes in size, as discussed in the section on two-precipitate simulations. The contour plots visually illustrate the simultaneous occurrence of precipitate coarsening and migration. We also observe that the velocity of precipitate migration is greater in the hotter regions than in the colder regions. Consequently, in regions with higher temperatures, thermomigration dominates, whereas in colder regions, Gibbs-Thomson coarsening takes precedence.

Figure 16(c-d) presents an enlarged view of the rectangular section indicated in Figure 16(a-b). It is evident that in the isothermal scenario (Figure 16(c)), the growth of the larger precipitate occurs at the expense of the smaller precipitate. Specifically, at time t_4 , the smaller precipitate has completely dissolved, while the central positions of these precipitates remain nearly unchanged throughout the process. In contrast, in the thermal gradient case (depicted in Figure 16(d)), the precipitate on the higher temperature side initiates migration. In this situation, both Ostwald ripening and thermomigration occur concurrently.

We conducted four sets of simulations with random precipitate distributions to determine the average center position (C_{avg}) for both the above-mentioned cases (isothermal and in the presence of thermal gradient). These four initial microstructures are provided in Section 5 of the supplementary material. We calculate the average center position of all precipitates over time for each set, and finally, we compute the average value of the center position by averaging the results from all four sets of simulations. In the isothermal case, as shown in Figure 16(e), C_{avg} remains relatively stable over time, indicating minimal movement. However, in the presence of a thermal gradient, C_{avg} shifts towards the higher temperature region, as shown in Figure 16(f). This shift in C_{avg} provides further evidence of the thermomigration of precipitates in addition to coarsening and shrinking.

5. Conclusion

- We developed a phase-field model to study the interplay between compositional and thermal gradients on microstructural evolution during thermomigration. The model is implemented in the MOOSE framework.
- Simulated composition profiles within single-phase regions of Fe-N and Fe-C alloys show a remarkable match with those obtained by Darken and Oriani in their classical experiments on thermal diffusion in these alloys. Further,

our simulated profiles compare well with the experimental results reported by Steiner in a Pb-Sn alloy where the thermal gradient spans both single and two-phase regions.

- In two-phase systems, thermomigration produces translational motion of precipitates towards the high-temperature region. The migration rate inversely varies with the size of the precipitate.
- The simulated composition profiles obtained from our study of thermomigration of a single precipitate show excellent agreement with the analytical solutions of our model.
- By conducting systematic simulations of thermomigration using two precipitates within a matrix subjected to a given thermal gradient, we ascertain that the choices between growth and shrinkage of precipitate depend on the inter-particle distance. Moreover, thermomigration can lead to inverse coarsening behavior leading to the growth of the smaller precipitate and the shrinkage of the larger one. It should be noted that such behaviour depends on the inter-particle distance. This observation is highly significant as it contrasts with the isothermal Ostwald-ripening behavior of precipitates.
- In multiple precipitate simulations, the presence of a thermal gradient induces thermomigration of precipitates in addition to capillarity-driven coarsening. When the thermal gradient is large, thermomigration dominates leading to the shift of the average center of mass of precipitates towards higher temperature regions.

In summary, our model accurately captures the coupled effects of thermomigration and diffusion-driven growth and coarsening of precipitates.

Acknowledgments

The authors acknowledge National Supercomputing Mission (NSM) for providing computing resources of “PARAM Sanganak” at IIT Kanpur and “PARAM Seva” at IIT Hyderabad, implemented by C-DAC and supported by the Ministry of Electronics and Information Technology (MeitY) and Department of Science and Technology (DST), Government of India. Rajdip Mukherjee acknowledges financial support from SERB core research grant (CRG/2019/006961). S.B. acknowledges financial support from DST-NSM Grant DST/NSM/R&D-HPC-Applications/2021/03. Soumya Bandyopadhyay thanks Indian Institute of Technology Kanpur for providing Institute Post Doctoral Fellowship.

Data Availability Statement

The data that support the findings of this study are available from the corresponding authors upon reasonable request.

CRedit authorship contribution statement

Sandip Guin: Conceptualization, Visualization, Methodology, Software, Investigation, Formal analysis, Validation, Data curation, Writing-Original Draft. **Soumya Bandyopadhyay:** Visualization, Methodology, Software, Investigation, Formal analysis, Validation, Data curation, Writing-Original Draft. **Saswata Bhattacharyya:** Supervision, Project administration, Resources, Writing - review & editing, Funding acquisition. & editing. **Rajdip Mukherjee:** Supervision, Project administration, Resources, Writing - review & editing, Funding acquisition.

Appendix A. Size change: Thermal migration

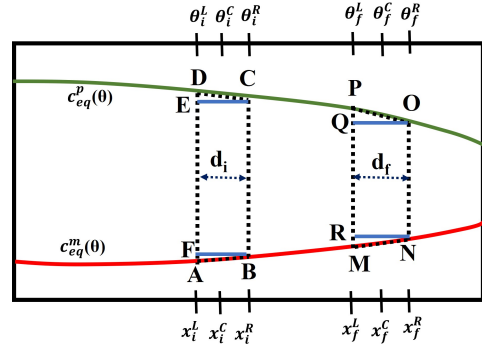


Figure A.17: Schematic of the composition profile in the matrix and precipitate phases under thermal gradient.

Let consider a flat interface precipitate of size= d_i inside a matrix under thermal gradient at time= t_i . Left interface of the precipitate is at X_i^L , right interface at X_i^R and center line at X_i^C . This initial system is shown in Fig Appendix A. Now due to migration, the precipitate migrated to a new higher temperature at Time= t_f and during the process size of the precipitate also changed to d_f . Now the Left interface of the precipitate is at X_f^L , right interface at X_f^R and center line at X_f^C . Temperature corresponding to point X_i^L , X_i^C , X_i^R , X_f^L , X_f^C and X_f^R is θ_i^L , θ_i^C , θ_i^R , θ_f^L , θ_f^C and θ_f^R . We plot the analytical 1D composition plot in Fig Appendix A, where ABCD region is precipitate at time= t_i and MNOP region is the precipitate at time= t_f .

If we consider AB and DC is linear At time = t_i , total area cover by ABCD region is given by:

$$A_i = d_i(AD + BC) \quad (\text{A.1})$$

$$AD = (c_{eq}^p(\theta = \theta_i^L) - c_{eq}^m(\theta = \theta_i^L)) \quad (\text{A.2})$$

$$BC = (c_{eq}^p(\theta = \theta_i^R) - c_{eq}^m(\theta = \theta_i^R)) \quad (\text{A.3})$$

replacing the values of Eq A.3 and Eq A.3 in Eq A.1

$$A_i = d_i((c_{eq}^p(\theta = \theta_i^L) - c_{eq}^m(\theta = \theta_i^L)) + (c_{eq}^p(\theta = \theta_i^R) - c_{eq}^m(\theta = \theta_i^R))) \quad (\text{A.4})$$

$$A_i = d_i((c_{eq}^p(\theta = \theta_i^L) + c_{eq}^p(\theta = \theta_i^R)) - (c_{eq}^m(\theta = \theta_i^L) + c_{eq}^m(\theta = \theta_i^R))) \quad (\text{A.5})$$

$$(c_{eq}^p(\theta = \theta_i^L) + c_{eq}^p(\theta = \theta_i^R)) = 2c_{eq}^p(\theta = \theta_i^C) \quad (\text{A.6})$$

$$(c_{eq}^m(\theta = \theta_i^L) + c_{eq}^m(\theta = \theta_i^R)) = 2c_{eq}^m(\theta = \theta_i^C) \quad (\text{A.7})$$

$$A_i = 2d_i(c_{eq}^p(\theta = \theta_i^C) - c_{eq}^m(\theta = \theta_i^C)) \quad (\text{A.8})$$

At time = t_f , total area cover by MNOP region is given by:

$$A_f = 2d_f(c_{eq}^p(\theta = \theta_f^C) - c_{eq}^m(\theta = \theta_f^C)) \quad (\text{A.9})$$

As the total composition of the system is constant, from Eq A.8 and Eq A.9 we can write

$$A_i = A_f \quad (\text{A.10})$$

$$d_f = d_i \frac{(c_{eq}^p(\theta = \theta_i^C) - c_{eq}^m(\theta = \theta_i^C))}{(c_{eq}^p(\theta = \theta_f^C) - c_{eq}^m(\theta = \theta_f^C))} \quad (\text{A.11})$$

$$\% \frac{d_f - d_i}{d_i} = \left\{ \frac{(c_{eq}^p(\theta = \theta_i^C) - c_{eq}^m(\theta = \theta_i^C))}{(c_{eq}^p(\theta = \theta_f^C) - c_{eq}^m(\theta = \theta_f^C))} - 1 \right\} * 100 \quad (\text{A.12})$$

References

- [1] L.S Darken and R.A Oriani. Thermal diffusion in solid alloys. *Acta Metallurgica*, 2(6):841–847, 1954.
- [2] Robert J Asaro, Diana Farkas, and Yashashree Kulkarni. The soret effect in diffusion in crystals. *Acta materialia*, 56(6):1243–1256, 2008.
- [3] Pierre Costesèque, Abdelkader Mojtabi, and Jean Karl Platten. Thermodiffusion phenomena. *Comptes Rendus Mécanique*, 339(5):275–279, 2011.
- [4] Gilbert LaRue Steiner. 1. *The Effect of a Temperature Gradient Upon Concentration in Binary Alloys*; 2. *The Effect of a Pressure Gradient Upon Concentration in Binary Alloys*. PhD thesis, Georgia Institute of Technology. Directed by William M. Spicer, 1957.
- [5] C Ludwig. Difusion awischen ungleich erwärmten orten gleich zusammengesetzter lösungen, 1856.
- [6] Jean Platten and Costeseque Pierre. Charles soret. a short biography: On the occasion of the hundredth anniversary of his death. *The European physical journal. E, Soft matter*, 15:235–9, 12 2004.
- [7] W. G. Whitman. Elimination of salt from sea-water ice. *American Journal of Science*, s5-11(62):126–132, 1926.
- [8] Yafeng Wang, Zhihua Xiao, Shenyang Hu, Yulan Li, and San-Qiang Shi. A phase field study of the thermal migration of gas bubbles in uo2 nuclear fuel under temperature gradient. *Computational Materials Science*, 183:109817, 2020.
- [9] P.F. Sens. The kinetics of pore movement in uo2 fuel rods. *Journal of Nuclear Materials*, 43(3):293–307, 1972.
- [10] WJ Chen, YA Zhou, SX Wang, FY Sun, and Yue Zheng. Phase field study the effects of interfacial energy anisotropy on the thermal migration of voids. *Computational Materials Science*, 159:177–186, 2019.
- [11] W.-C. Yang, H. Ade, and R. J. Nemanich. Stability and dynamics of Pt-Si liquid microdroplets on Si(001). *Phys. Rev. B*, 69:045421, Jan 2004.
- [12] Michael Meier, Mark J. Harrison, Steven Spalsbury, and Douglas S. Mc-Gregor. Laser-induced thermomigration of Te precipitates in CdZnTe crystals. *Journal of Crystal Growth*, 311(17):4247–4250, 2009.
- [13] A. Zappettini, N. Zambelli, G. Benassi, D. Calestani, and M. Pavesi. Live-monitoring of Te inclusions laser-induced thermo-diffusion and annealing in CdZnTe crystals. *Applied Physics Letters*, 104(25):252105, 06 2014.
- [14] Swanand Pawar, Kerry P. Wang, Andrew Yeckel, and Jeffrey J. Derby. Analysis of temperature gradient zone melting and the thermal migration of liquid particles through a solid. *Acta Materialia*, 228:117780, 2022.
- [15] Long-Qing Chen. Phase-field models for microstructure evolution. *Annual Review of Materials Research*, 32(1):113–140, 2002.
- [16] M. Verma, S. Sugathan, S. Bhattacharyya, and R. Mukherjee. Effect of concurrent thermal grooving and grain growth on morphological and topological evolution of a polycrystalline thin film: Insights from a 3d phase-field study. *Acta Materialia*, 261:119393, 2023.
- [17] Soumya Bandyopadhyay, Vishal Panwar, Sandip Guin, Anoop C R, Nilesh Prakash Gurao, and Rajdip Mukherjee. Multivariant microstructure evolution in Ti-alloys: insights from a quantitative phase-field study. *Modelling and Simulation in Materials Science and Engineering*, 31(6):065019, aug 2023.
- [18] Vincent Feyen and Nele Moelans. Quantitative high driving force phase-field model for multi-grain structures. *Acta Materialia*, 256:119087, 2023.
- [19] Supriyo Chakraborty, Praveen Kumar, and Abhik Choudhury. Phase-field modeling of grain-boundary grooving and migration under electric current and thermal gradient. *Acta Materialia*, 153:377–390, 2018.
- [20] Vahid Attari and Raymundo Arróyave. Phase-field study of thermomigration in 3-d ic micro interconnects. *IEEE Transactions on Components, Packaging and Manufacturing Technology*, 10(9):1466–1473, 2020.
- [21] Kamalath Kadirvel, Hamish L. Fraser, and Yunzhi Wang. Microstructural design via spinodal-mediated phase transformation pathways in high-entropy alloys (heas) using phase-field modelling. *Acta Materialia*, 243:118438, 2023.
- [22] Arjun Varma R., Prita Pant, and M.P. Gururajan. Dislocation assisted phase separation: A phase field study. *Acta Materialia*, 244:118529, 2023.
- [23] Wenkun Wu, Ursula R. Kattner, Carelyn E. Campbell, Jonathan E. Guyer, Peter W. Voorhees, James A. Warren, and Olle G. Heinonen. Co-based superalloy morphology evolution: A phase field study based on experimental thermodynamic and kinetic data. *Acta Materialia*, 233:117978, 2022.
- [24] Long-Qing Chen. Phase-field models for microstructure evolution. *Annual review of materials research*, 32(1):113–140, 2002.
- [25] Ingo Steinbach. Phase-field models in materials science. *Modelling and simulation in materials science and engineering*, 17(7):073001, 2009.
- [26] M Verma and R Mukherjee. Grain growth stagnation in solid state thin films: A phase-field study. *Journal of Applied Physics*, 130(2):025305, 2021.
- [27] Rashmi R Mohanty, Jonathan E Guyer, and Yong Ho Sohn. Diffusion under temperature gradient: A phase-field model study. *Journal of applied physics*, 106(3):034912, 2009.
- [28] Liangzhe Zhang, Michael R Tonks, Paul C Millett, Yongfeng Zhang, Karthikeyan Chockalingam, and Bulent Biner. Phase-field modeling of temperature gradient driven pore migration coupling with thermal conduction. *Computational materials science*, 56:161–165, 2012.
- [29] Vahid Attari and Raymundo Arróyave. Phase-field study of thermomigration in 3-d ic micro interconnects. *IEEE Transactions on Components, Packaging and Manufacturing Technology*, 10(9):1466–1473, 2020.
- [30] Shuibao Liang, Cheng Wei, and Changbo Ke. Effect of anisotropy in thermal conductivity on grain boundary migration under temperature gradient—a phase field study. *Materials Letters*, 303:130517, 2021.
- [31] John W Cahn. On spinodal decomposition. *Acta metallurgica*, 9(9):795–801, 1961.
- [32] ED Eastman. Thermodynamics of non-isothermal systems. *Journal of the American Chemical Society*, 48(6):1482–1493, 1926.
- [33] Dan Zhao, Alois Würger, and Xavier Crispin. Ionic thermoelectric materials and devices. *Journal of Energy Chemistry*, 61:88–103, 2021.
- [34] Chih Chen, Hsiang-Yao Hsiao, Yuan-Wei Chang, Fanyi Ouyang, and King-Ning Tu. Thermomigration in solder joints. *Materials Science and Engineering: R: Reports*, 73(9-10):85–100, 2012.
- [35] Roy H Stogner, Graham F Carey, and Bruce T Murray. Approximation of cahn–hilliard diffuse interface models using parallel adaptive mesh refinement and coarsening with c1 elements. *International journal for numerical methods in engineering*, 76(5):636–661, 2008.

- [36] Michael R Tonks, Derek Gaston, Paul C Millett, David Andrs, and Paul Talbot. An object-oriented finite element framework for multiphysics phase field simulations. *Computational Materials Science*, 51(1):20–29, 2012.
- [37] Alexander D. Lindsay, Derek R. Gaston, Cody J. Permann, Jason M. Miller, David Andrs, Andrew E. Slaughter, Fande Kong, Joshua Hansel, Robert W. Carlsen, Casey Icenhour, Logan Harbour, Guillaume L. Giudicelli, Roy H. Stogner, Peter German, Jacob Badger, Sudipta Biswas, Leora Chapuis, Christopher Green, Jason Hales, Tianchen Hu, Wen Jiang, Yeon Sang Jung, Christopher Matthews, Yinbin Miao, April Novak, John W. Peterson, Zachary M. Prince, Andrea Rovinelli, Sebastian Schunert, Daniel Schwen, Benjamin W. Spencer, Swetha Veeraraghavan, Antonio Recuero, Dewen Yushu, Yaqi Wang, Andy Wilkins, and Christopher Wong. 2.0 - MOOSE: Enabling massively parallel multiphysics simulation. *SoftwareX*, 20:101202, 2022.
- [38] K.X. Yin, Z.W. Huang, B.L. Wu, G.J. Zhang, Q.W. Tian, and Y.N. Wang. Prediction of phase stabilities of solid solutions for high entropy alloys. *Acta Materialia*, 263:119445, 2024.
- [39] Stanislaw M Dubiel and Jakub Cieslak. Sigma-phase in Fe-Cr and Fe-V alloy systems and its physical properties. *Critical reviews in solid state and materials sciences*, 36(4):191–208, 2011.
- [40] R. Mukherjee, T.A. Abinandanan, and M.P. Gururajan. Phase field study of precipitate growth: Effect of misfit strain and interface curvature. *Acta Materialia*, 57(13):3947–3954, 2009.
- [41] Jae-Gil Jung, Amir R. Farkoosh, and David N. Seidman. Microstructural and mechanical properties of precipitation-strengthened Al-Mg-Zr-Sc-Er-Y-Si alloys. *Acta Materialia*, 257:119167, 2023.
- [42] Christoph M. Hell, Bjørn Holmedal, Ruben Bjørge, Calin D. Marioara, and Randi Holmestad. The microstructural origin of a hardness double-peak in an age-hardened en-aw 6082. *Acta Materialia*, 256:119095, 2023.
- [43] Danan Fan, S.P. Chen, Long-Qing Chen, and P.W. Voorhees. Phase-field simulation of 2-d ostwald ripening in the high volume fraction regime. *Acta Materialia*, 50(8):1895–1907, 2002.

Supplementary Material

Interplay between thermal and compositional gradients decides the microstructure during thermomigration: a phase-field study

Sandip Guin^{†a,b}, Soumya Bandyopadhyay^{†a,c}, Saswata Bhattacharyya^{d,*}, Rajdip Mukherjee^{a,*}

^aDepartment of Materials Science and Engineering, Indian Institute of Technology, Kanpur, Kanpur-208016, UP, India

^bInternational College of Semiconductor Technology, National Yang Ming Chiao Tung University, Hsinchu 300, Taiwan

^cDepartment of Materials Science and Engineering, University of Florida, Gainesville, Florida-32611

^dDepartment of Materials Science And Metallurgical Engineering , Indian Institute of Technology, Hyderabad , Sangareddy - 502285, Telangana, India

arXiv:2406.00649v1 [cond-mat.mtrl-sci] 2 Jun 2024

1. Single-phase system

Darken and Orani demonstrated the evolution of concentration gradient in single phase Fe-N and Fe-C alloys due to the presence of thermal gradient [1]. To simulate their experimental results, we extracted the Gibbs free energy density data for the entire temperature range. For example, for the Fe-N sample, we have considered temperatures ranging from 600°C to 756°C. For this temperature range, we have extracted the Gibbs free energy density vs composition data at different temperatures ranging from 600°C to 756°C using Calphad-based Thermocalc software [? ?]. We have converted all these data into dimensionless values.

The composition is scaled between 0 and 1 using the following equation;

$$c' = \frac{N(\text{at}\%) - c_{\min}}{c_{\max} - c_{\min}}, \quad (1)$$

here, c' is dimensionless form of concentration, $c_{\min} = 0.002\text{at}\%$ and $c_{\max} = 0.5\text{at}\%$. The initial N concentration in the experimental case is 0.021 at% [1]. The temperature is scaled using the following equation;

$$\theta = \frac{T - T_{\min}}{T_{\max} - T_{\min}}, \quad (2)$$

here, θ is dimensionless form of temperature, $T_{\min} = 600^\circ\text{C}$ and $T_{\max} = 756^\circ\text{C}$. For the experimental case, the temperature range is from 622°C ($\theta = 0.14$) to 756°C ($\theta = 1.0$). The free energy density is scaled using the following equation,

$$f'(c', \theta) = \frac{f(c, T) - f_{\min}}{f_{\max} - f_{\min}}, \quad (3)$$

here, $f'(c', \theta)$ is the scaled form of free energy density, $f_{\min} = f(0.5\text{at}\%, 756^\circ\text{C})$ and $f_{\max} = f(0.002\text{at}\%, 600^\circ\text{C})$. Then, we have fitted $f'(c', \theta)$ into a function of c' and θ , which is given by;

$$f'(c', \theta) = Pc'^2 + Qc' + R, \quad (4)$$

here, $P = -0.0028\theta^2 + 0.0046\theta + 0.0049$, $Q = -0.0054\theta - 0.0186$ and $R = -0.9637\theta + 1.0759$. Figure 1(a) shows the $f'(c', \theta)$ surface plot as function of c' and θ . It is clearly visible that, with increasing θ , $f'(c', \theta)$ value decreases. With increasing c' , $f'(c', \theta)$ also decreases, but this change is not clearly visible from the plot. For that reason, we have plotted a 1D profile of $f'(c', \theta)$ vs. c' for $\theta = 0.4, 0.5, 0.6$ (shown in Figure 1b).

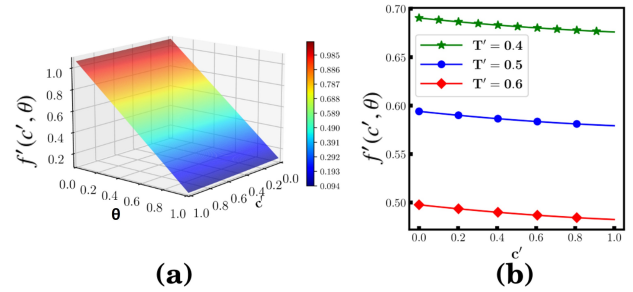


Figure 1: (a) $f'(c', \theta)$ plot as function of both c' and θ . (b) $f'(c', \theta)$ vs c' plot at $\theta = 0.4, 0.5$ and 0.6 .

We extracted the temperature-dependent mobility of N in α -Fe phase for Fe-N systems using the MOBHEA2 database in Thermocalc software [?]. We have scaled these mobility values and used these scaled values as M_c in Equation:15 in the main article. Figure 2(a) shows actual temperature-dependent mobility while, Figure 2(b) shows the scaled mobility. It is visible from these figures that, the increment of mobility with temperature is similar for both actual and scaled mobility. In our simulation we, used the $M_c(\text{scaled}) = 0.611\theta^2 + 0.1714\theta + 0.1749$.

For Fe-C, system we have done similar process as explained in the case for Fe-N system. We have extracted the Gibbs free energy density for the temperature range from 550°C to 690°C. Initial C concentration is 0.016at%. We did the dimensionless conversion following the method as explained for Fe-N case. In this case $T_{\min} = 550^\circ\text{C}$, $T_{\max} = 690^\circ\text{C}$, $c_{\min} = 0.002\text{at}\%$, $c_{\max} = 0.5\text{at}\%$, $f_{\min} = f(0.5\text{at}\%, 690^\circ\text{C})$

*Corresponding Authors

Email addresses: saswata@msme.iitk.ac.in (Saswata Bhattacharyya), rajdipm@iitk.ac.in (Rajdip Mukherjee)

†These authors contributed equally to this work

and $f_{max} = f(0.002at\%, 550^\circ C)$. Here also, we used scaled mobility of C in α -Fe phase in our main simulation.

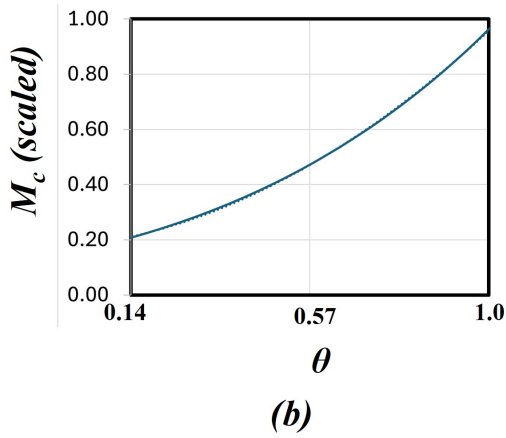
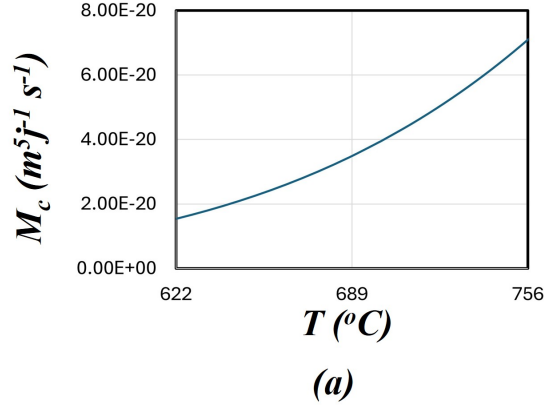


Figure 2: (a) $M_c(m^5 J^{-1} s^{-1})$ vs. $T(^{\circ}C)$ plot for N in α -Fe. (b) Scaled mobility plot wrt. scaled temperature (θ) for the same system.

For both cases, we use a simulation domain of $100\Delta X \times 40\Delta Y$, where initial concentration for N is at homogenous 0.021at% and for C is 0.016 at%. Constant temperature gradient is applied within the simulation domain, ranging from $622^\circ C$ to $756^\circ C$ for Fe-N system and $554^\circ C$ to $690^\circ C$ for Fe-C system. For both Fe-N and Fe-C system we take κ_c to be 1.0.

2. Pb-Sn system

For the Pb-Sn system, the bulk free energy density is taken as;

$$f(c, T) = A(c_i - c_{eq_i}^\alpha(T))^2(c_i - c_{eq_i}^\beta(T))^2, \quad (5)$$

here, $c_{eq_i}^\alpha(T)$ represents the equilibrium Sn concentration of the α phase as a function of temperature, while $c_{eq_i}^\beta(T)$ represents the equilibrium Sn concentration of the β phase as a function of temperature. We have previously discussed the scaling of composition and temperature. Here, T_{min} is equal to $101^\circ C$ ($\theta = 0$), and T_{max} is equal to $210^\circ C$ ($\theta = 1$). Therefore, C_{min} corresponds to the equilibrium Sn concentration of the α phase at $101^\circ C$

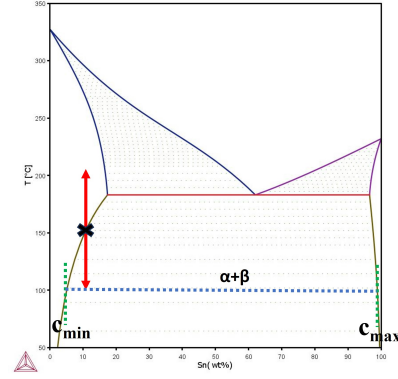


Figure 3: Pb-Sn phase diagram [4].

($\theta = 0$), and C_{max} corresponds to the equilibrium Sn concentration of the β phase at $101^\circ C$ ($\theta = 0$). T_{min} is equal to $101^\circ C$, and T_{max} is equal to $210^\circ C$. Pb-Sn phase diagram is shown in Figure 3. Therefore, the final scaled free energy density can be expressed as follows;

$$f'(c', \theta) = A(c'_i - (0.0181 + 0.1605\theta^2))^2 (c'_i - (0.9983 - 0.0146\theta^2))^2. \quad (6)$$

We conducted four sets of simulations and obtained the average results for comparison with the experimental data. At the initial time, the temperature is set to be the minimum temperature ($T = T_{min}$). The initial microstructure consists of two domains: single phase-phase region and two-phase region. In single-phase region, the Sn concentration is kept 14wt%, while in two-phase region we randomly placed β precipitate with the α matrix. Here the volume fraction of the β precipitate is according to the equilibrium volume fraction of β precipitate at $T = T_{min}$ and 14 wt% Sn concentration. Figure 4 shows the initial microstructure of one of simulations. Hence, the initial Sn concentration at this point was set to 14wt%. After that, we apply the thermal gradient in the system.

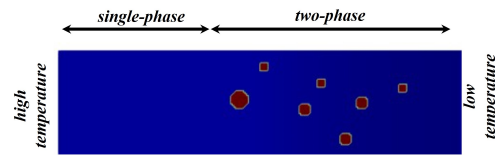


Figure 4: Initial microstructure for Pb-Sn simulation

In this case, we have also used the scaled mobility of Sn in Pb-Sn system. Figures 5(a) shows the mobility of Sn in Pb-Sn system wrt. temperature, while Figures 5(b) shows the scaled mobility for the same. In this case mobility of Sn in Pb-Sn system has been calculated using the MOBHEA2 database in Thermocalc software [?]. In our simulation, $M_c(scaled) = 4.02\theta^3 - 3.73\theta^2 + 1.009\theta - 0.0557$. In this case our simulation size is For both cases, we use a simulation domain of

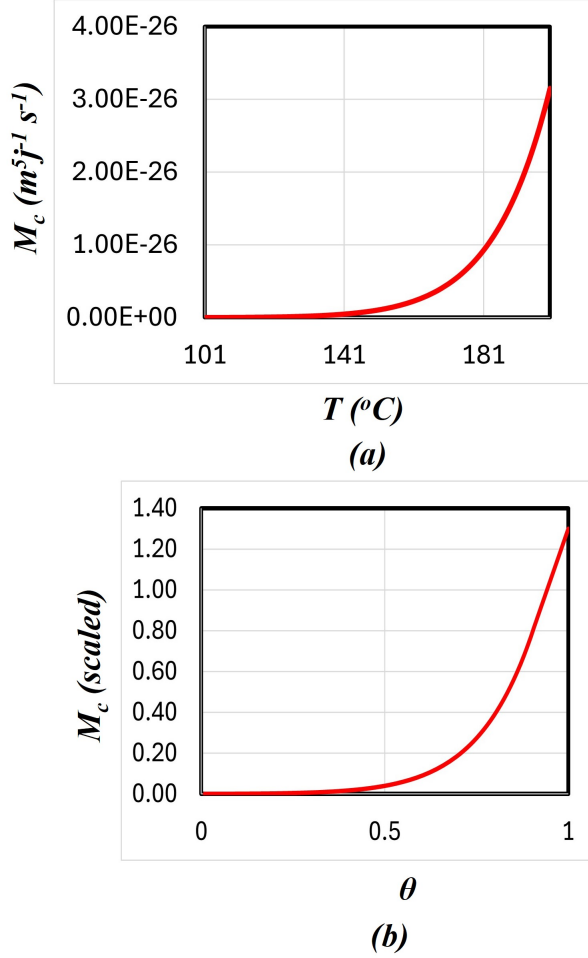


Figure 5: (a) $M_c(m^5 J^{-1} s^{-1})$ vs. $T(^{\circ}C)$ plot for Sn in Pb-Sn system. (b) Scaled mobility plot wrt. scaled temperature (θ) for the same system.

$512\Delta X \times 128\Delta Y$. Here we consider κ_c to be 1.0 for our simulation. We run four simulation with different initial condition and take the average 1D composition plot which we have shown in the Figure 7b of main article. In all four simulations, only the initial position of the β precipitates in the two-phase region are different. Figure 4 shows one of the microstructure of such simulation.

3. Fe-V system system

In this case, we followed a process similar to the Pb-Sn system, as discussed in the previous section (Section 3). However, in this case, C_{min} corresponds to the equilibrium V concentration of the α phase at $834^{\circ}C$, and C_{max} corresponds to the equilibrium V concentration of the σ phase at $1056^{\circ}C$. Additionally, T_{min} is equal to $834^{\circ}C$, and T_{max} is equal to $1056^{\circ}C$. Therefore, the final scaled free energy density can be expressed as follows;

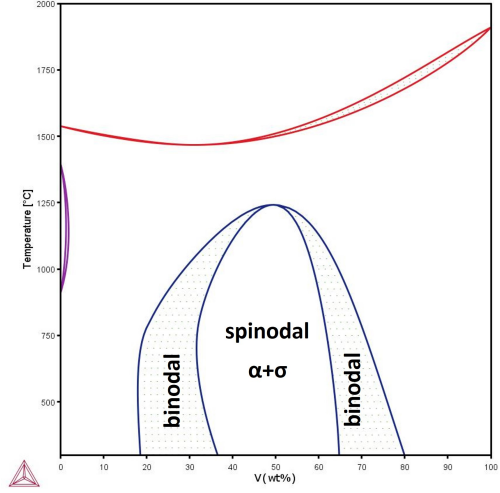


Figure 6: Fe-V phase diagram

$$f'(c', \theta) = A(c'_i - (0.9959 + 0.0170\theta - 1.4359\theta^2 + 2.5796\theta^3 - 1.5812\theta^4))^2 + (c'_i - (0.0053 + 0.0292\theta + 1.3499\theta^2 - 2.2324\theta^3 + 1.3674\theta^4))^2, \quad (7)$$

here, we take $A=1.0$. The value of $\kappa_c = 1.0$ and $M_c = 1.0$ in Equation:15 in the main article. The simulation domain size is $1024\Delta X \times 1024\Delta Y$.

4. Case:B of two precipitate simulation

Figure 7 shows the evolution of each precipitate diameter with time for the Case:B of two precipitate simulations. In this case, P_1 and P_2 represent the left (lower temperature) and right (higher temperature) precipitate, respectively.

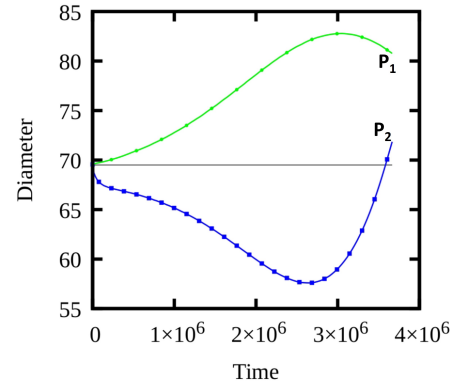


Figure 7: Evolution of each precipitate size with time for Case:B of two precipitate simulations.

5. Multi-Precipitate simulations

In this case, we simulated four microstructures for both isothermal and thermal gradient cases. Precipitates are randomly placed inside the matrix. These initial microstructures are shown in Figure 8. Here, the red circles represent the precipitates, and the blue region is the matrix.

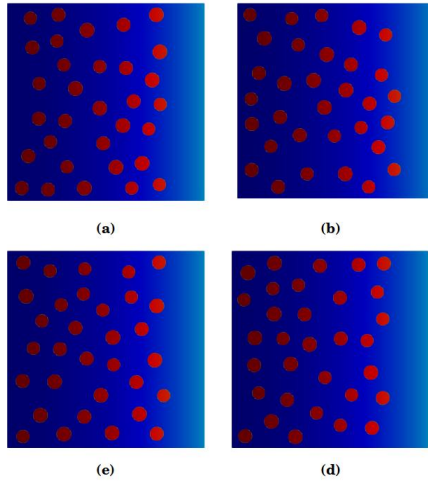


Figure 8: Four sets of initial microstructure for multi-precipitates simulation.

References

- [1] L.S Darken and R.A Oriani. Thermal diffusion in solid alloys. *Acta Metallurgica*, 2(6):841–847, 1954.
- [2] Robert J Asaro, Diana Farkas, and Yashashree Kulkarni. The soret effect in diffusion in crystals. *Acta materialia*, 56(6):1243–1256, 2008.
- [3] Pierre Costesèque, Abdelkader Mojtabi, and Jean Karl Platten. Thermodiffusion phenomena. *Comptes Rendus Mécanique*, 339(5):275–279, 2011.
- [4] Gilbert LaRue Steiner. 1. *The Effect of a Temperature Gradient Upon Concentration in Binary Alloys*; 2. *The Effect of a Pressure Gradient Upon Concentration in Binary Alloys*. PhD thesis, Georgia Institute of Technology. Directed by William M. Spicer, 1957.
- [5] C Ludwig. Difusion awischen ungleich erwärmten orten gleich zusammengesetzter lösungen, 1856.
- [6] Jean Platten and Costeseque Pierre. Charles soret. a short biography: On the occasion of the hundredth anniversary of his death. *The European physical journal. E, Soft matter*, 15:235–9, 12 2004.
- [7] W.G. Whitman. Elimination of salt from sea-water ice. *American Journal of Science*, s5-11(62):126–132, 1926.
- [8] Yafeng Wang, Zhihua Xiao, Shenyang Hu, Yulan Li, and San-Qiang Shi. A phase field study of the thermal migration of gas bubbles in uo2 nuclear fuel under temperature gradient. *Computational Materials Science*, 183:109817, 2020.
- [9] P.F. Sens. The kinetics of pore movement in uo2 fuel rods. *Journal of Nuclear Materials*, 43(3):293–307, 1972.
- [10] WJ Chen, YA Zhou, SX Wang, FY Sun, and Yue Zheng. Phase field study the effects of interfacial energy anisotropy on the thermal migration of voids. *Computational Materials Science*, 159:177–186, 2019.
- [11] W.-C. Yang, H. Ade, and R. J. Nemanich. Stability and dynamics of Pt-Si liquid microdroplets on Si(001). *Phys. Rev. B*, 69:045421, Jan 2004.
- [12] Michael Meier, Mark J. Harrison, Steven Spalsbury, and Douglas S. McGregor. Laser-induced thermomigration of Te precipitates in CdZnTe crystals. *Journal of Crystal Growth*, 311(17):4247–4250, 2009.
- [13] A. Zappettini, N. Zambelli, G. Benassi, D. Calestani, and M. Pavesi. Live-monitoring of Te inclusions laser-induced thermo-diffusion and annealing in CdZnTe crystals. *Applied Physics Letters*, 104(25):252105, 06 2014.
- [14] Swanand Pawar, Kerry P. Wang, Andrew Yeckel, and Jeffrey J. Derby. Analysis of temperature gradient zone melting and the thermal migration of liquid particles through a solid. *Acta Materialia*, 228:117780, 2022.
- [15] Long-Qing Chen. Phase-field models for microstructure evolution. *Annual Review of Materials Research*, 32(1):113–140, 2002.
- [16] M. Verma, S. Sugathan, S. Bhattacharyya, and R. Mukherjee. Effect of concurrent thermal grooving and grain growth on morphological and topological evolution of a polycrystalline thin film: Insights from a 3d phase-field study. *Acta Materialia*, 261:119393, 2023.
- [17] Soumya Bandyopadhyay, Vishal Panwar, Sandip Guin, Anoop C R, Nilesh Prakash Gurao, and Rajdip Mukherjee. Multivariant microstructure evolution in Ti-alloys: insights from a quantitative phase-field study. *Modelling and Simulation in Materials Science and Engineering*, 31(6):065019, aug 2023.
- [18] Vincent Feyen and Nele Moelans. Quantitative high driving force phase-field model for multi-grain structures. *Acta Materialia*, 256:119087, 2023.
- [19] Supriyo Chakraborty, Praveen Kumar, and Abhik Choudhury. Phase-field modeling of grain-boundary grooving and migration under electric current and thermal gradient. *Acta Materialia*, 153:377–390, 2018.
- [20] Vahid Attari and Raymundo Arróyave. Phase-field study of thermomigration in 3-d ic micro interconnects. *IEEE Transactions on Components, Packaging and Manufacturing Technology*, 10(9):1466–1473, 2020.
- [21] Kamalnath Kadirvel, Hamish L. Fraser, and Yunzhi Wang. Microstructural design via spinodal-mediated phase transformation pathways in high-entropy alloys (heas) using phase-field modelling. *Acta Materialia*, 243:118438, 2023.
- [22] Arjun Varma R., Prita Pant, and M.P. Gururajan. Dislocation assisted phase separation: A phase field study. *Acta Materialia*, 244:118529, 2023.
- [23] Wenkun Wu, Ursula R. Kattner, Carelyn E. Campbell, Jonathan E. Guyer, Peter W. Voorhees, James A. Warren, and Olle G. Heinonen. Co-based superalloy morphology evolution: A phase field study based on experimental thermodynamic and kinetic data. *Acta Materialia*, 233:117978, 2022.

- [24] Long-Qing Chen. Phase-field models for microstructure evolution. *Annual review of materials research*, 32(1):113–140, 2002.
- [25] Ingo Steinbach. Phase-field models in materials science. *Modelling and simulation in materials science and engineering*, 17(7):073001, 2009.
- [26] M Verma and R Mukherjee. Grain growth stagnation in solid state thin films: A phase-field study. *Journal of Applied Physics*, 130(2):025305, 2021.
- [27] Rashmi R Mohanty, Jonathan E Guyer, and Yong Ho Sohn. Diffusion under temperature gradient: A phase-field model study. *Journal of applied physics*, 106(3):034912, 2009.
- [28] Liangzhe Zhang, Michael R Tonks, Paul C Millett, Yongfeng Zhang, Karthikeyan Chockalingam, and Bulent Biner. Phase-field modeling of temperature gradient driven pore migration coupling with thermal conduction. *Computational materials science*, 56:161–165, 2012.
- [29] Vahid Attari and Raymundo Arróyave. Phase-field study of thermomigration in 3-d ic micro interconnects. *IEEE Transactions on Components, Packaging and Manufacturing Technology*, 10(9):1466–1473, 2020.
- [30] Shuibao Liang, Cheng Wei, and Changbo Ke. Effect of anisotropy in thermal conductivity on grain boundary migration under temperature gradient—a phase field study. *Materials Letters*, 303:130517, 2021.
- [31] John W Cahn. On spinodal decomposition. *Acta metallurgica*, 9(9):795–801, 1961.
- [32] ED Eastman. Thermodynamics of non-isothermal systems. *Journal of the American Chemical Society*, 48(6):1482–1493, 1926.
- [33] Dan Zhao, Alois Würger, and Xavier Crispin. Ionic thermoelectric materials and devices. *Journal of Energy Chemistry*, 61:88–103, 2021.
- [34] Chih Chen, Hsiang-Yao Hsiao, Yuan-Wei Chang, Fanyi Ouyang, and King-Ning Tu. Thermomigration in solder joints. *Materials Science and Engineering: R: Reports*, 73(9-10):85–100, 2012.
- [35] Roy H Stogner, Graham F Carey, and Bruce T Murray. Approximation of cahn–hilliard diffuse interface models using parallel adaptive mesh refinement and coarsening with c1 elements. *International journal for numerical methods in engineering*, 76(5):636–661, 2008.
- [36] Michael R Tonks, Derek Gaston, Paul C Millett, David Andrs, and Paul Talbot. An object-oriented finite element framework for multiphysics phase field simulations. *Computational Materials Science*, 51(1):20–29, 2012.
- [37] Alexander D. Lindsay, Derek R. Gaston, Cody J. Permann, Jason M. Miller, David Andrs, Andrew E. Slaughter, Fande Kong, Joshua Hansel, Robert W. Carlsen, Casey Icenhour, Logan Harbour, Guillaume L. Giudicelli, Roy H. Stogner, Peter German, Jacob Badger, Sudipta Biswas, Leora Chapuis, Christopher Green, Jason Hales, Tianchen Hu, Wen Jiang, Yeon Sang Jung, Christopher Matthews, Yinbin Miao, April Novak, John W. Peterson, Zachary M. Prince, Andrea Rovinelli, Sebastian Schunert, Daniel Schwen, Benjamin W. Spencer, Swetha Veeraraghavan, Antonio Recuero, Dewen Yushu, Yaqi Wang, Andy Wilkins, and Christopher Wong. 2.0 - MOOSE: Enabling massively parallel multiphysics simulation. *SoftwareX*, 20:101202, 2022.
- [38] K.X. Yin, Z.W. Huang, B.L. Wu, G.J. Zhang, Q.W. Tian, and Y.N. Wang. Prediction of phase stabilities of solid solutions for high entropy alloys. *Acta Materialia*, 263:119445, 2024.
- [39] Stanisław M Dubiel and Jakub Cieślak. Sigma-phase in Fe-Cr and Fe-V alloy systems and its physical properties. *Critical reviews in solid state and materials sciences*, 36(4):191–208, 2011.
- [40] R. Mukherjee, T.A. Abinandanan, and M.P. Gururajan. Phase field study of precipitate growth: Effect of misfit strain and interface curvature. *Acta Materialia*, 57(13):3947–3954, 2009.
- [41] Jae-Gil Jung, Amir R. Farkoosh, and David N. Seidman. Microstructural and mechanical properties of precipitation-strengthened Al-Mg-Zr-Sc-Er-Y-Si alloys. *Acta Materialia*, 257:119167, 2023.
- [42] Christoph M. Hell, Bjørn Holmedal, Ruben Bjørge, Calin D. Marioara, and Randi Holmestad. The microstructural origin of a hardness double-peak in an age-hardened en-aw 6082. *Acta Materialia*, 256:119095, 2023.
- [43] Danan Fan, S.P. Chen, Long-Qing Chen, and P.W. Voorhees. Phase-field simulation of 2-d ostwald ripening in the high volume fraction regime. *Acta Materialia*, 50(8):1895–1907, 2002.